JM PAPERS

The characterization of the particle normal stresses of concentrated granular suspensions by local rheometry

Enzo d'Ambrosio[1], Frédéric Blanc[1] and Elisabeth Lemaire[1],†

[1]InPhyNi-UMR 7010, Université Côte d'Azur, CNRS, 06108 Nice Cedex 2, France

The normal and shear viscosities of non-Brownian suspensions are measured by optical suspension imaging for particle volume fractions ϕ between $0.3\phi_m$ and $0.98\phi_m$, where ϕ_m is the jamming fraction. Two distinct refractive-index-matched suspensions, made with the same polymethyl methacrylate spherical particles dispersed in a mixture of water and Triton X-100, are studied. One is density-matched while the other one is negatively buoyant. They are both sheared in a Couette rheometer where the velocity and particle volume fraction fields are measured. The shear viscosity and the second particle normal stress Σ_{22}^p are determined through the study of these profiles in the neutrally buoyant suspension, while the third particle normal stress Σ_{33}^p is deduced from the analysis of the vertical ϕ profiles measured in the negatively buoyant suspension. Our results indicate that the shear viscosity decreases with shear stress Σ_{12}, and that this shear-thinning behaviour can be captured by the variation of ϕ_m with Σ_{12}. We show that Σ_{33}^p is proportional to Σ_{12}, and that $\Sigma_{33}^p/\eta_0\dot{\gamma}$ is a function of only $\phi/\phi_m(\Sigma_{12})$. The values of Σ_{22}^p deduced from the radial ϕ profiles are consistent with the results of Zarraga *et al.* (*J. Rheol.*, vol. 44, 2000, pp. 185–220). We conclude by discussing our results in the framework of the $\mu(J)$ rheology for viscous numbers J ranging from 2×10^{-4} to 3×10^1. We obtain very good agreement with the results obtained by Boyer *et al.* for $J \lesssim 10^{-1}$ (*Phys. Rev. Lett.*, vol. 107, 2011, 188301) and by Zarraga *et al.* for $J \gtrsim 10^{-1}$.

Key words: suspensions, particle/fluid flow, rheology

1. Introduction

Non-Brownian suspensions are widespread in industry (paints, fresh concrete, solid rocket propellants, etc.) as well as in biological (blood) and natural (mud, lava, submarine

† Email address for correspondence: elisabeth.lemaire@unice.fr

avalanche, etc.) flows, to mention but a few. This widespread presence of suspensions has encouraged active research in the past years that has revealed great complexity in the behaviour of these systems. Even the simplest suspensions, non-Brownian suspensions made of rigid single-sized spherical particles suspended in a Newtonian fluid and sheared in a viscous creeping flow, can exhibit a rich variety of complex behaviours, including shear-thinning (Lobry *et al.* 2019) and shear-thickening (Barnes 1989; Mari *et al.* 2014; Guy, Hermes & Poon 2015; Comtet *et al.* 2017), normal stress differences, irreversibility under oscillating shear (Pine *et al.* 2005), shear-induced microstructure (Gadala-Maria & Acrivos 1980; Blanc, Peters & Lemaire 2011; Blanc *et al.* 2013) and particle migration (Phillips *et al.* 1992; Ovarlez, Bertrand & Rodts 2006; Snook, Butler & Guazzelli 2016; Sarabian *et al.* 2019). In the last decade, the central role played by direct solid contacts on the flow properties of suspensions has been revealed. Boyer, Guazzelli & Pouliquen (2011) succeeded in applying a granular paradigm to describe the rheological behaviour of non-Brownian and non-colloidal spheres suspended in a Newtonian fluid, showing the key role played by contact interactions between particles. The proliferation of frictional contacts is also known to be responsible for the discontinuous shear-thickening (DST) that is observed in very dense suspensions (Mari *et al.* 2014; Wyart & Cates 2014) when the shear stress is high enough to overcome repulsive interactions between particles and push them into contact. Finally, numerical simulations (Lobry *et al.* 2019) and experimental studies (Chatté *et al.* 2018; Arshad *et al.* 2021; Le *et al.* 2023) have also shown that the shear-thinning regime observed for concentrated frictional suspensions (i.e. beyond the DST) could be related to a variable friction coefficient between particles.

Batchelor (1970) showed that the total stress can be divided into two contributions:

$$\boldsymbol{\Sigma} = \boldsymbol{\Sigma}^f + \boldsymbol{\Sigma}^p. \tag{1.1}$$

Here, $\boldsymbol{\Sigma}^f$ is the stress related to the suspending fluid, given by $\boldsymbol{\Sigma}^f = -(1 - \phi)p\boldsymbol{I} + 2\eta_0\dot{\boldsymbol{\epsilon}}$, p denotes the hydrodynamic pressure, η_0 is the viscosity of the suspending fluid, and $\dot{\boldsymbol{\epsilon}}$ is the strain rate tensor. Also, $\boldsymbol{\Sigma}^p$, known as the particle stress, gathers the contributions of the particles in the form of hydrodynamic and solid direct contact interactions.

The deviatoric part of the stress tensor can be written as $\Sigma_{12} = 2\eta_0(1 + \eta_s^p)\dot{\epsilon}_{12}$, where η_s^p describes the particle contribution to the relative shear viscosity of the suspension: $\eta_s = 1 + \eta_s^p$. Many phenomenological equations relating the suspension viscosity to the particle volume fraction can be found in the literature (von Eilers 1941; Maron & Pierce 1956; Quemada 1998; Zarraga, Hill & Leighton 2000; Mills & Snabre 2009). All of them include a divergence of the viscosity when the particle volume fraction approaches a critical value ϕ_m, with a law of the type $\eta_s \propto (1 - \phi/\phi_m)^{-n}$ for $n \approx 2$.

Among other transport properties, shear-induced particle migration has received increasing attention in recent decades. If this phenomenon can be due to inertial effects (Segre & Silberberg 1962), then it can also occur in the viscous regime (at low Reynolds numbers). At first, it was considered that solid particles tended to migrate to the lowest shear regions of the flow. For instance, the particles have been observed to migrate towards the centre of the channel in a Poiseuille flow (Koh, Hookham & Leal 1994; Hampton *et al.* 1997; Butler & Bonnecaze 1999; Snook *et al.* 2016) or towards the outer cylinder in a wide-gap Couette flow (Abbott *et al.* 1991; Graham *et al.* 1991; Chow *et al.* 1994; Sarabian *et al.* 2019). However, this migration towards the low-shear regions is not systematic. For instance, an outward migration has been observed in cone-and-plate geometry (Chow *et al.* 1995) despite a constant shear rate in this type of geometry. Conversely, the experiments of Chapman (1991), Chow *et al.* (1994) and Merhi *et al.* (2005) show that migration in

parallel-plate torsional flow is weak or zero although the shear rate increases linearly with the radial distance from the centre.

Another typical example of shear-induced migration is the viscous resuspension whereby an initially settled layer of negatively buoyant particles expands vertically when a shear flow is applied. Observed for the first time by Gadala-Maria & Acrivos (1980), it was then explained by Leighton & Acrivos (1986) and Acrivos, Mauri & Fan (1993), who demonstrated that the height of the resuspended particle layer results from the balance between a downward gravitational flux and an upward shear-induced diffusion flux. Later, Zarraga *et al.* (2000) revisited the results of Acrivos *et al.* (1993) to determine the particle normal stress in the vorticity direction, denoted Σ_{33}^p. They showed that $\Sigma_{33}^p/\eta_s\dot{\gamma}$ is a function of the solid volume fraction scaling as $\phi^3 \exp(2.34\phi)$, where η_s, $\dot{\gamma}$ and ϕ are the relative shear viscosity, shear rate and volume fraction, respectively. More recent experiments (Saint-Michel *et al.* 2019; d'Ambrosio, Blanc & Lemaire 2021), based on the determination of Σ_{33}^p from the measurement of the vertical volume fraction profiles, have supported the main results of Zarraga *et al.* (2000). However, they have also shown a surprising scaling where Σ_{33}^p varies with the shear rate following a power law with an exponent close to 0.7. We will come back to this unexpected scaling in § 6.

Nott & Brady (1994) proposed to relate the particle migration flux $j_\perp$ to the particle pressure gradient. This model was then refined by Morris & Boulay (1999), who considered the anisotropy of the particle normal stresses and established the well-known suspension balance model (SBM):

$$j_\perp = \frac{2a^2}{9\eta_s} f(\phi)(\nabla \cdot \Sigma^p + \phi \, \Delta\rho \, g), \tag{1.2}$$

where a is the particle radius, and $\Delta\rho$ is the density difference between the particles and the suspending fluid. Also, $f(\phi)$ is the hindrance function that characterizes the decrease of the sedimentation rate of a homogeneous suspension of spheres at a given solid volume fraction ϕ compared to the Stokes settling velocity of an isolated particle (Richardson & Zaki 1954):

$$f(\phi) = (1 - \phi)^\alpha, \quad \text{with } \alpha \approx 4\text{–}5. \tag{1.3}$$

According to the SBM (Morris & Boulay 1999), the particle stress tensor is written as

$$\Sigma^p = -\eta_0\dot{\gamma} \, Q(\phi) + 2\eta_0 \, \eta_s^p(\phi) \, \dot{\epsilon}, \quad \text{with } Q = \eta_n^p(\phi) \, \hat{Q} = \eta_n^p(\phi) \begin{pmatrix} 1 & 0 & 0 \\ 0 & \lambda_2^p & 0 \\ 0 & 0 & \lambda_3^p \end{pmatrix}, \tag{1.4}$$

where η_n^p is known as relative normal viscosity and is defined as the ratio $-\Sigma_{11}^p/\eta_0\dot{\gamma}$. Morris & Boulay (1999) propose the following expression for η_n^p:

$$\eta_n^p = K_n \left(\frac{\phi/\phi_m}{1 - \phi/\phi_m} \right)^2, \tag{1.5}$$

with $K_n = 0.75$ and $\phi_m = 0.68$. Later, Gallier *et al.* (2014) fitted this function to their numerical results and obtained $K_n = 1.13$ and $\phi_m = 0.58$, in the case of frictional suspensions with interparticle friction coefficient 0.5. These results are close to the experimental values obtained by Dbouk, Lobry & Lemaire (2013) ($K_n = 1.1$ and $\phi_m = 0.58$) and by Boyer *et al.* (2011) ($K_n = 1$ and $\phi_m = 0.585$).

In (1.4), the tensor $\hat{Q}$ describes the anisotropy of the particle normal stresses. Morris & Boulay (1999) showed that taking $\lambda_3^p = 0.5$ and $\lambda_2^p \approx 0.8$ enabled capture of the

main features of shear-induced particle migration in all the considered flow geometries (wide-gap Couette flow, parallel-plate flow and cone-and-plate flow), even though the SBM should probably be refined to account for a ϕ dependency of λ_2^p and λ_3^p. These numerical values were later confirmed by numerical (Gallier *et al.* 2014) and experimental (Dbouk *et al.* 2013) studies, which both show a mild dependence of these coefficients on ϕ.

Lhuillier (2009) and Nott, Guazzelli & Pouliquen (2011) updated the SBM by suggesting that only the contribution coming from direct contacts between particles, denoted $\boldsymbol{\Sigma}^c$, should be considered instead of $\boldsymbol{\Sigma}^p$. The exact nature of the particle normal stresses that intervene in shear-induced migration is still an open question, much beyond the scope of the present paper. In the following, we will use the notations Σ_{ii}^p, η_n and λ_i to denote the stresses involved in the particle migration, without presuming their origin.

An alternative viewpoint of concentrated suspension rheology has been proposed by Boyer *et al.* (2011), who showed that the rheological behaviour of highly concentrated suspension ($\phi > 0.45$) can be described entirely by a macroscopic friction coefficient μ, defined as $\mu(J) = \Sigma_{12}/P^p$, and the volume fraction $\phi(J)$, both of them being functions of the dimensionless viscous number J:

$$J = \frac{\eta_0 \dot{\gamma}}{P^p}, \tag{1.6}$$

where P^p is the particle pressure, defined as $P^p = \eta_n(\phi)\,\eta_0\dot{\gamma}$. Thanks to a sophisticated home-made experimental device, they carried out measurements at imposed particle pressure on very dense suspensions ($J \in [10^{-6}, 2 \times 10^{-1}]$) by imposing the shear stress and the particle pressure at the same time while the volume fraction of the suspension adapts to these solicitations. By imposing a very small shear stress and a large particle pressure, their experimental device has allowed them to explore the range of extremely high particle volume fractions ($\phi_m - \phi \sim 10^{-3}$). They proposed a constitutive law where μ can be divided into two contributions:

$$\mu = \mu^C + \mu^H. \tag{1.7}$$

Here, μ^C and μ^H are respectively the hydrodynamic contribution and the contact contribution, defined as

$$\mu^C = \mu_1 + \frac{\mu_2 - \mu_1}{1 + I_0/J} \quad \text{and} \quad \mu^H = J + \frac{5}{2}\phi_m J^{1/2}, \tag{1.8a,b}$$

with $\mu_1 = 0.32$, $\mu_2 = 0.7$ and $I_0 = 0.005$. For $\phi(J)$, the following expression has been proposed:

$$\phi(J) = \frac{\phi_m}{1 + J^{1/n}}, \quad \text{with } n = 2. \tag{1.9}$$

These experiments have been repeated by Tapia, Pouliquen & Guazzelli (2019), Dagois-Bohy *et al.* (2015) and Etcheverry (2022), who obtained qualitatively the same results and confirmed that the asymptotic behaviour of μ and ϕ in the vicinity of the jamming transition can be written as

$$\left.\begin{array}{l} \mu - \mu_c \propto J^{1/2}, \\ \phi_m - \phi \propto J^{1/2}, \end{array}\right\} \tag{1.10}$$

where μ_c is the quasi-static value of the effective friction coefficient. These results have been supported globally by the numerical simulations of Gallier *et al.* (2014) and

Chèvremont, Chareyre & Bodiguel (2019), despite a slight discrepancy in the range of high viscous number (when the concentration decreases).

In this paper, we also aim to characterize the rheological behaviour of non-Brownian frictional suspensions over a broad range of concentrations and stresses. The suspensions and the experimental method are depicted in § 2. The fields of velocity $v(r, z)$ and particle volume fraction $\phi(r, z)$ that will be used further to determine the rheological behaviour of the suspensions are presented in § 3. In §§ 4 and 5, we study the local rheological behaviour of the neutrally buoyant suspension for different averaged concentrations $\bar{\Phi}$. The constitutive law $\eta_s(\phi/\phi_m)$, together with the variation of ϕ_m with the shear stress, is presented in § 4, while we establish the constitutive law $q_2 = 1/\mu = \Sigma_{22}^p/\Sigma_{12}$ as a function of the solid volume fraction ϕ in § 5. In § 6, we revisit a previous work that aimed to study viscous resuspension (d'Ambrosio *et al.* 2021). We show that, as expected, Σ_{33}^p is proportional to the shear stress, and that the ratio $\Sigma_{33}^p/\Sigma_{12}$ is a function of only ϕ/ϕ_m. Finally, in § 7, we compare our results with the literature in the framework of the $\mu(J)$ rheology.

2. Materials and methods

In the following, we describe the two suspensions used to study the rheological behaviour of non-Brownian frictional suspensions: a density-matched suspension, denoted as suspension A, and a second suspension made of the same particles dispersed in a less-dense fluid, denoted as suspension B. These two suspensions are very similar to each other. Both are made of the same spherical polymethyl methacrylate (PMMA) particles (Arkema BS572) suspended in a Newtonian liquid which is composed of mostly Triton X-100. Furthermore, the two suspensions are sheared in the same experimental set-up (d'Ambrosio *et al.* 2021), a wide-gap Couette cell, and the local rheology methods used to characterize both suspensions are also the same.

2.1. *Suspensions*

2.1.1. *Density-matched suspension A*
PMMA spheres (Arkema BS572) of diameter $2a = 268 \pm 25\,\mu\text{m}$ and density $(1.19 \pm 0.01) \times 10^3\,\text{kg m}^{-3}$ are used. The particles are dispersed in a mixture composed of 73.86 wt % of Triton X-100, 14.24 wt % of zinc chloride and 11.90 wt % of water (Souzy *et al.* 2015; Souzy, Pham & Metzger 2016), with a small amount of fluorescent dye (Nile Blue A, Sigma-Aldrich). This mixture is Newtonian with viscosity $\eta_0^{(A)} = 5.0 \pm 0.3\,\text{Pa s}$, measured in a rotational plate geometry at working temperature $T = 20\,^{\circ}\text{C}$. The liquid and the particles are chosen to have almost the same refractive index, 1.49, and the same density. Accurate index matching is achieved by tuning the temperature (Christiansen 1884) of the chamber that contains the rheometer, in order to have a transparent suspension.

2.1.2. *Suspension B of negatively buoyant particles*
In the case of the negatively buoyant suspension B, the same particles (Arkema BS 572) are used but they are now dispersed in a mixture composed of 99 wt % of Triton X-100 and 1 wt % of water saturated in Nile Blue A (d'Ambrosio *et al.* 2021). This mixture is Newtonian with viscosity $\eta_0^{(B)} = 0.34 \pm 0.02\,\text{Pa s}$ and density
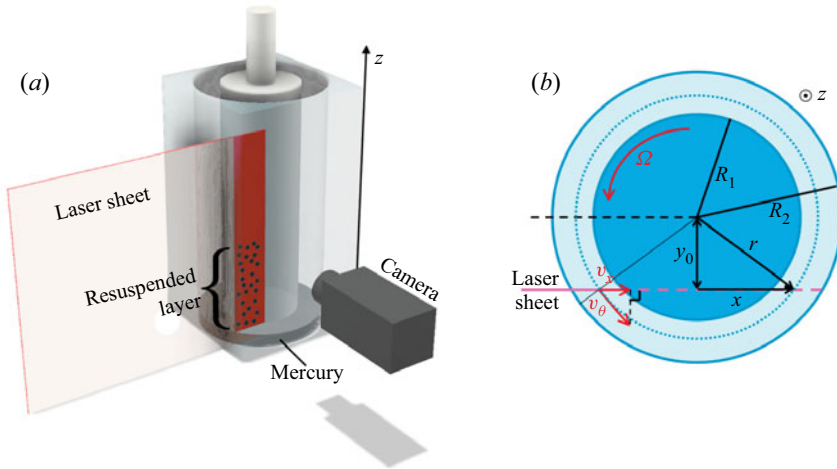
Figure 1. (*a*) Sketch of the experimental device used to characterize suspensions A and B. (Note that in the case of suspension A, there is no 'resuspended layer' since the suspension is density-matched.). (*b*) View from above. The vertical laser sheet is shifted by a distance $y_0 < R_1$ from the radial plane (dashed black line). Here, x is the horizontal position in the laser sheet, and z is the vertical position, with $z = 0$ set by the mercury/suspension interface. In this paper, directions denoted by 1, 2 and 3 will refer to the θ, r and z directions, respectively.

$(1.06 \pm 0.01) \times 10^3 \, \text{kg m}^{-3}$. The liquid and the particles are shown to have the same refractive index when the temperature of the chamber is set to $T = 23\,^\circ\text{C}$.

2.2. *Device*

The experimental device is the same as used by d'Ambrosio *et al.* (2021). Suspensions A and B are sheared in a Couette cell of height 10 cm, made of PMMA mounted on a controlled-stress rheometer (Mars II Thermofisher) (see figure 1*a*). The inner cylinder has radius $R_1 = 19$ mm and rotates at constant angular velocity Ω, while the outer cylinder (stator) has radius $R_2 = 24$ mm. In this configuration, the gap is much larger than the particle diameter $((R_2 - R_1)/(2a) \approx 18)$, and the shear stress variation over the gap is expected to be of the order of $\Sigma_{12}(R_1)/\Sigma_{12}(R_2) = R_2^2/R_1^2 \approx 1.6$. Considering the radial variation of the shear stress in the gap, an outward migration of the particles is expected (Phillips *et al.* 1992) for the density-matched suspension A, which prevents characterization of the rheology of the suspension from usual macroscopic measurements. Furthermore, as will be discussed in § 3, we observe particle layering near the walls, which again makes the macroscopic rheology measurements irrelevant.

The bottom of the Couette cell is first filled with mercury in order to prevent particle migration towards the region located under the rotor and to maximize the suspension slip at the bottom to get a shear rate as homogeneous as possible in the vertical direction (Leighton & Acrivos 1987). The suspension is then poured into the cup, and the rotor is slowly moved down to approximately 2 mm from the cup bottom so that it dips into the mercury. The suspension is illuminated by a thin vertical laser sheet (thickness $\approx 50\,\mu\text{m}$) shifted by offset $y_0 = 16.6$ mm from the radial plane for the suspension A, and $y_0 = 16.2$ mm for suspension B (see figure 1*b*). A camera (IDS UI-3290SE-M-GL) is positioned at 90° from the enlightened plane. The solid particles appear as black disks in the camera frame. The accurate matching of the refractive index, the thinness of the

967 A34-6

laser sheet and the resolution of the camera allow the recording of high-quality images with resolution 30 px per particle.

2.3. *Measurement methods*

2.3.1. *Concentration fields*

For both suspensions (A and B), the method used to measure the concentration field is the same as in d'Ambrosio *et al.* (2021). The concentration field is determined through the measurement of the particle number density n_{ij} in the (x, z) vertical laser plane. To this aim, each image is binarized with a local threshold whose value $T(x, z)$ is calculated individually for each pixel (x, z) of the image $I(x, z)$, where $T(x, z)$ is a weighted sum (cross-correlation with a Gaussian window) of a 171 px × 171 px neighbourhood of the pixel (x, z). The particles are detected through a watershed segmentation process (Vincent & Soille 1991), and the position of the barycentre of each segmented zone gives the position of each particle centre in the (x, z) plane sampled with rectangular cells (i, j) with edges of sizes δx and δz. One can note that δx can be adapted to the purpose of the measurement. For instance, a high resolution allows us to observe particle layering near the walls but is not required to study the outward migration of particles, where the concentration is expected to vary smoothly. For the vertical direction, we have chosen $\delta z \sim 2a$ in order to measure $\phi(z)$ with a high spatial resolution.

In each cell $[\delta x \times \delta z]$, the number of particle centres $N_{ij}(x, z)$ is measured. The particle density $n_{ij}(r, z) = N_{ij}/(\delta x \, \delta y)$ is reconstructed in the (r, z) plane, making the change of variable $r = \sqrt{y_0^2 + x^2}$. Due to the non-zero thickness of the laser sheet and the slight polydispersity of the particles, n_{ij} is not the absolute particle density, and to compute the true particle volume fraction ϕ, we use particle volume conservation: $\phi(r, z) = \chi \, n(r, z)$. Depending on the type of suspension (neutrally (A) or negatively (B) buoyant particles), the coefficient χ is determined either from the total height H of the suspension imaged by the camera for suspension A, or from the sediment height in the gap, h_0, and the value of the packing volume fraction of the sediment, ϕ_0, for suspension B:

$$\chi_A = \frac{\pi \bar{\Phi}(R_2^2 - R_1^2)H}{\int_0^H \int_{R_1}^{R_2} n_{ij} 2\pi r \, dr \, dz} \quad \text{and} \quad \chi_B = \frac{\pi \phi_0 (R_2^2 - R_1^2)h_0}{\int_0^{h_0} \int_{R_1}^{R_2} n_{ij} 2\pi r \, dr \, dz}, \tag{2.1a,b}$$

where H is the height of suspension A, $\bar{\Phi}$ is the averaged solid volume fraction in suspension A, $h_0 = 21.3 \, \text{mm} \approx 4(R_2 - R_1)$ is the sediment height in suspension B, and $\phi_0 = 0.574 \pm 0.003$ is the packing fraction of the sediment (see d'Ambrosio *et al.* 2021). Finally, $\phi(r, z)$ is averaged over 10 000 non-correlated images (see figures 2(*a*) and 4*a*).

2.3.2. *Velocity fields*

The same numerical process is applied to measure the velocity field for both kinds of suspensions. The shift in the laser sheet out of the radial plane allows particle image velocimetry (PIV) measurements (Manneville, Bécu & Colin 2004) in the (x, z) plane. Under the assumption that the radial component of the velocity is much smaller than the azimuthal component, v_θ can be deduced from a simple projection of v_x along the
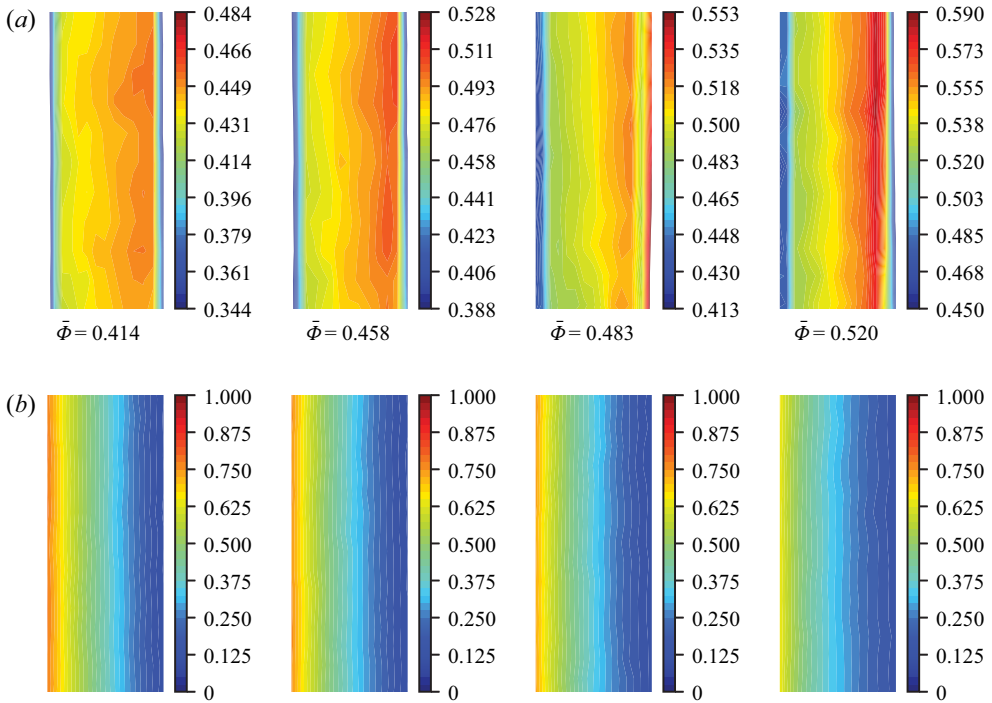
Figure 2. (*a*) Particle volume fraction maps: examples of solid volume fraction mappings for four different average concentrations of suspension A, namely $\bar{\Phi} = 0.414, 0.458, 0.483$ and 0.520. (*b*) Normalized orthoradial velocity maps: examples of relative velocity mappings $v_\theta/\Omega R_1$ for $\Omega = 1$ rpm for the same $\bar{\Phi}$ as in (*a*). The inner cylinder (rotor) is located on the left of each map, while the outer cylinder (stator) is on the right. Horizontal resolution is $\delta x = 1/14(R_2 - R_1)$.

orthoradial direction (see figure 1*b*):

$$v_\theta(x, z) = v_x(x, z)\,\frac{\sqrt{x^2 + y_0^2}}{y_0}. \tag{2.2}$$

The velocity field $\boldsymbol{v}(v_x(x, z), v_z(x, z))$ is computed using the open source software DPIVSOFT (available at https://www.irphe.fr/meunier; Meunier & Leweke 2003). Each image is divided into correlation windows of size $128\,\text{px} \times 128\,\text{px}$. Each correlation window contains approximately 10 particles that play the role of PIV tracers. The cross-correlation of the corresponding windows from two successive images yields the mean velocity of the particles in the window. The in-plane loss of pairs error is decreased by translating the correlation windows in a second run (Westerweel 1997), thus reducing the correlation window size to $64\,\text{px} \times 64\,\text{px}$. The same procedure performed on all windows gives the velocity field, which is averaged over 100 images. The mapping of the θ component of the velocity field in the (x, z) plane is then obtained and used to reconstruct the velocity field in the (r, z) plane (see figures 2(*b*) and 4(*b*)).

3. Concentration and velocity profiles

3.1. *Neutrally buoyant suspension A*

Steady radial profiles of particle volume fraction were measured for several values of $\bar{\Phi} = 0.520, 0.500, 0.483, 0.458, 0.435, 0.414, 0.394$. To measure these profiles, the
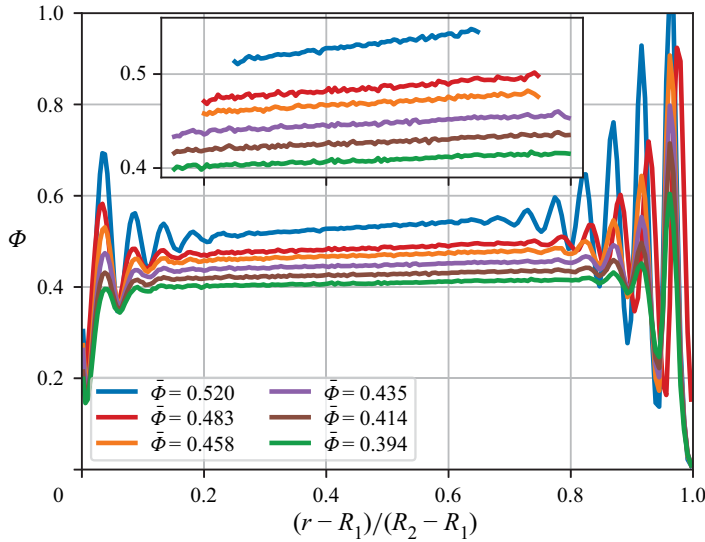
967 A34-8

Figure 3. Steady radial profiles of the volume fraction $\phi(r)$ for the different average volume fractions $\bar{\Phi}$. Two main observations can be made in agreement with the literature: (1) the particle layering near the walls, which tends to be larger when $\bar{\Phi}$ increases; (2) the outward migration of the particles, which appears to be even more pronounced when $\bar{\Phi}$ is higher. The inset shows a zoom of the profiles outside the zones where particle layering is observed. Horizontal resolution is $\delta x = (R_2 - R_1)/200$.

suspension is first sheared at a constant inner cylinder rotation speed $\Omega = 1$ rpm. Throughout the shearing process, the torque to be applied to the inner cylinder to maintain a constant rotation rate is recorded, and when it no longer varies, the migration steady state is considered to have been reached. The typical time and accumulated strain before recording the concentration and velocity fields are of the order of 8 h and 12 000, respectively. Figure 2(*a*) displays examples of concentration mappings for four different values of $\bar{\Phi}$: 0.414, 0.458, 0.483 and 0.52. One can observe that, as expected, the solid volume fraction ϕ is vertically homogeneous, while a clear outside migration is visible as well as a decay of ϕ near the walls. These maps are averaged vertically to obtain the radial ϕ profiles, shown in figure 3. In agreement with the literature, we observe particle layering that is more and more pronounced as $\bar{\Phi}$ increases (Yeo & Maxey 2010; Blanc *et al.* 2013; Metzger, Rahli & Yin 2013; Gallier *et al.* 2016; Deboeuf *et al.* 2018; Sarabian *et al.* 2019). The decay in ϕ near the walls displayed in figure 2(*a*) is related to this layering.

Once the concentration profile has been measured at $\Omega = 1$ rpm, the velocity profiles are measured for several angular speeds of the inner cylinder, $\Omega = 0.1, 0.2, 0.3, 0.5, 0.7,$ $1, 2$ rpm, in order to study the rheological behaviour of the suspension over a large range of shear stress $\Sigma_{12} \in [2, 170]$ Pa. The Reynolds number and the Taylor number are smaller than 1 for all the values of the applied angular velocity (for the highest angular velocity, $Re = \rho \Omega R_1 (R_2 - R_1)/\eta \sim 10^{-2}$ and $Ta = 4\rho^2 \Omega^2 (R_2 - R_1)^4/\eta^2 \sim 10^{-5}$), and the Péclet number is very large ($Pe = 6\pi \eta a^3 \dot{\gamma}/k_B T > 10^{10}$). Examples of velocity fields $v_\theta(r, z)/\Omega R_1$ are presented in figure 2(*b*). As observed for the particle concentration field, v_θ does not vary with z. The z-averaged radial profiles $v_\theta(r)$ are shown in Appendix A (figure 12) for each average concentration $\bar{\Phi}$ and each rotor velocity Ω. The velocity profiles are increasingly deviating from a Newtonian profile as the average concentration

$\bar{\Phi}$ increases, in agreement with the literature (Ovarlez *et al.* 2006). Besides, it is observed that the wall slip is more and more significant when $\bar{\Phi}$ increases or when Ω decreases.

3.2. *Negatively buoyant suspension B*

When the particles are heavier than the suspending liquid, they settle. Under the application of a shear stress, the settled layer expands, resulting in an inhomogeneous vertical concentration profile. We focus on the steady profiles, obtained when the resuspension is completed, for various angular velocities $\Omega = 0.3, 0.5, 1, 2, 5, 10, 20, 30, 40, 60$ rpm. The suspension B is first sheared with an angular velocity of the rotor equal to 5 rpm for one hour. Then Ω is set to the desired value, and the torque applied to the inner cylinder is registered. The acquisition of images begins when the torque becomes constant (after a few hours, which corresponds to a strain of approximately 10^4). For all the experiments, the Reynolds number and the Taylor number are smaller than 1, and the Péclet number is very large ($Pe > 10^8$). These procedures are described more thoroughly in d'Ambrosio *et al.* (2021), along with the main results that are as follows.

(i) Particle layering is also observed near the walls over a distance of approximately $8a \approx (R_2 - R_1)/5$ for $\phi \approx 0.55$.
(ii) Outside these zones, the particle volume fraction hardly varies along r at given z, in contrast with what has been observed for the neutrally buoyant suspension.
(iii) The concentration decreases slowly with z in the resuspended layer, and drops sharply to zero at the clear liquid/suspension interface.

These results are illustrated in figure 4.

4. Shear viscosity

The purpose of this section is to describe how the relationship between the shear stress and the shear rate is determined for different particle volume fractions through local measurements in the neutrally buoyant suspension (A). It is worth mentioning that the vertical gradient of concentration that is present in the negatively buoyant suspension (B) precludes the determination of the shear stress from the torque applied to the rotor.

4.1. *Local viscosity measurement method*

The stress field is obtained by solving the Cauchy momentum equation, which for low-Reynolds-number flows (see § 3 for evaluation of the Reynolds number) reduces to

$$\nabla \cdot \boldsymbol{\Sigma} = 0, \tag{4.1}$$

which gives

$$\Sigma_{12} = \Sigma_{\theta r} = \frac{C}{r^2}, \quad \text{with } C = \frac{\Gamma}{2\pi H}, \tag{4.2}$$

where H and Γ are the height of the suspension in the gap and the torque applied on the rotor, respectively. Then from the measurement of the velocity profiles $v_\theta(r)$, we determine

(*a*)

$\Omega = 0$ rpm $\Omega = 0.3$ rpm $\Omega = 2.0$ rpm $\Omega = 20.0$ rpm $\Omega = 60.0$ rpm
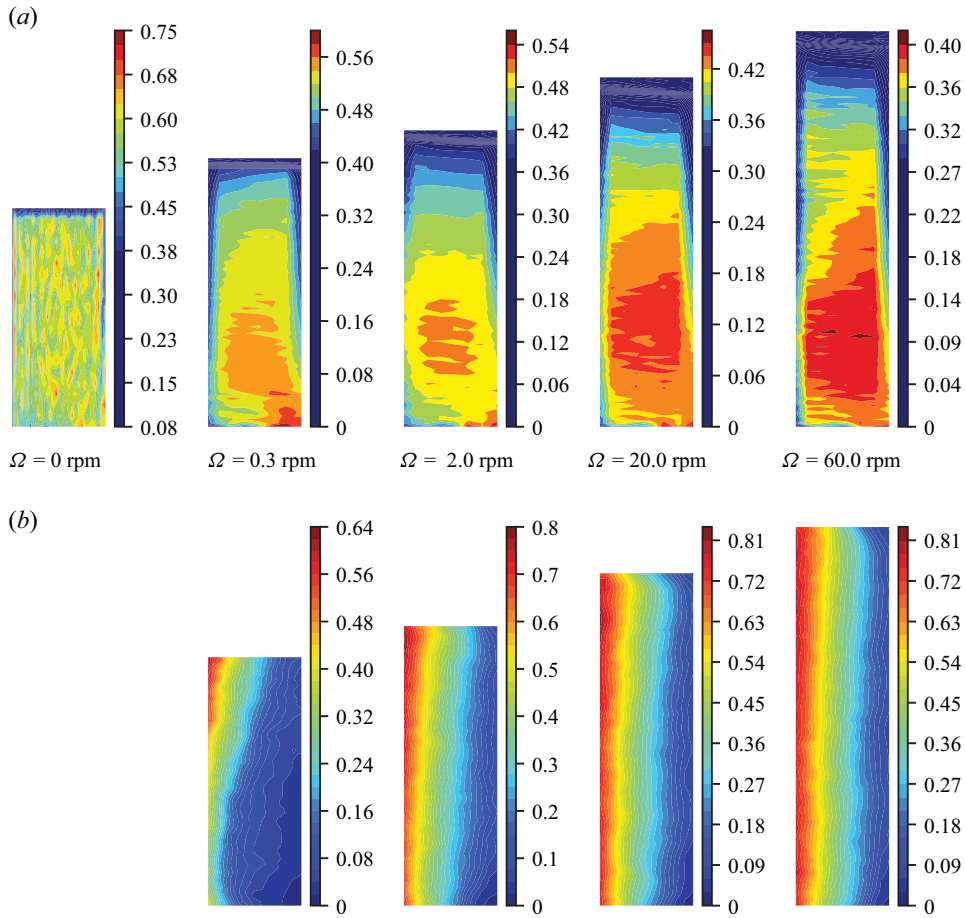
(*b*)

Figure 4. Volume fraction and orthoradial velocity maps in the resuspension experiments with suspension B for different rotor angular velocity values. (*a*) Particle volume fraction maps: mapping of the particle volume fraction averaged over 10 000 images (with the exception of $\Omega = 0$ rpm, for which only 20 images have been averaged). (*b*) Normalized orthoradial velocity maps: azimuthal velocity normalized by the rotor velocity and averaged over 100 velocity fields. Figure from d'Ambrosio *et al.* (2021).

the local relative shear viscosity:

$$\eta_s(r) = \frac{\Sigma_{12}}{\eta_0 \dot{\gamma}}, \tag{4.3}$$

with

$$\dot{\gamma} = -r \frac{\partial(v_\theta/r)}{\partial r}. \tag{4.4}$$

The viscosity of the suspension is determined outside the layered zones near the walls (see figure 3) since it is well-known that particle layering significantly affects the rheological behaviour (Gallier *et al.* 2014, 2016) of suspensions. To obtain the variation of the shear viscosity η_s with the shear stress and the particle volume fraction, the shear rate $\dot{\gamma}(r)$ is determined for each radial position (using (4.4)) as well as the particle volume fraction $\phi(r)$, while the local shear stress $\Sigma_{12}(r)$ is given by (4.2). The analysis of all these

967 A34-11

data shows that, at a given value of ϕ, the suspension behaves as a non-Newtonian shear-thinning fluid (see appendix B).

4.2. *Shear-thinning behaviour captured by a stress-dependent jamming volume fraction*

Flow curves of shear-thinning suspensions are sometimes fitted by a Herschel–Bulkley law (Coussot & Piau 1994; Schatzmann, Fischer & Bezzola 2003; Sosio & Crosta 2009; Mueller, Llewellin & Mader 2010; Vance, Sant & Neithalath 2015). This approach is depicted briefly in Appendix B. However, a more convenient way to capture shear-thinning consists in introducing a stress-dependent jamming volume fraction, $\phi_m(\Sigma_{12})$ (Wildemuth & Williams 1984; Zhou, Uhlherr & Luo 1995; Blanc *et al.* 2018; Lobry *et al.* 2019). The value of ϕ_m at a given stress is obtained by measuring the variation of the relative viscosity with the volume fraction, which, as displayed in figure 5, can be adjusted by a Maron–Pierce law:

$$\eta_r(\Sigma_{12}) = \left(1 - \frac{\phi}{\phi_m(\Sigma_{12})}\right)^{-2}. \tag{4.5}$$

More precisely, we obtained the variation of ϕ_m with Σ_{12} by fitting the variation of $1/\sqrt{\eta_r}$ with ϕ at a given shear stress. Figure 15 in Appendix C shows these fittings for different values of the local shear stress. It is worth noting that the Maron–Pierce law, although globally adequate to represent the variation of the viscosity with the volume fraction, is not respected perfectly for the largest volume fractions for which the exponent tends to decrease. A better fit could have been obtained by introducing, as is often done (Blanc *et al.* 2018; Singh *et al.* 2018; Lobry *et al.* 2019), a second free parameter in the Maron–Pierce law: $\eta_r(\Sigma_{12}) = \alpha(\Sigma_{12})(1 - \phi/\phi_m(\Sigma_{12}))^{-2}$. However, we have chosen to limit the number of free parameters in the constitutive law in order to facilitate the analysis of the data that will be presented below, in particular in §§ 6 and 7. Furthermore, figure 5 shows that with this one-parameter fitting, the experimental data approximately line up on a single curve, which provides a consistency check for the fitting procedure.

The variation of ϕ_m with Σ_{12} is displayed in figure 6, where it is observed that ϕ_m increases from 0.54 to 0.59 when the shear stress increases from 5 to 90 Pa, illustrating the shear-thinning behaviour of the suspension. Besides, one can note that the values of ϕ_m are in the typical range reported in the literature for frictional non-Brownian suspensions (Zarraga *et al.* 2000; Ovarlez *et al.* 2006; Boyer *et al.* 2011; Peters *et al.* 2016; Singh *et al.* 2018; Blanc *et al.* 2018; Lobry *et al.* 2019; Arshad *et al.* 2021). In figure 6, we have also plotted a power-law fitting curve (black line) that will be used in the following when we need to estimate the local value of the jamming fraction, knowing the local value of the stress:

$$\phi_m = 0.515 \, \Sigma_{12}^{0.0286}. \tag{4.6}$$

This power law is valid only on the shear stress domain that has been investigated, and has no physical meaning. It would have been possible to fit our data by a law of the type of Lobry *et al.* (2019), which corresponds to a variation of ϕ_m with stress driven by a decrease in the pairwise friction coefficient when Σ_{12} increases. Indeed, the range of variation of ϕ_m with Σ_{12} is fully consistent with what is predicted for shear-thinning induced by a variable friction coefficient between particles. But for the sake of simplicity in data analysis, we chose the simple power law of (4.6).
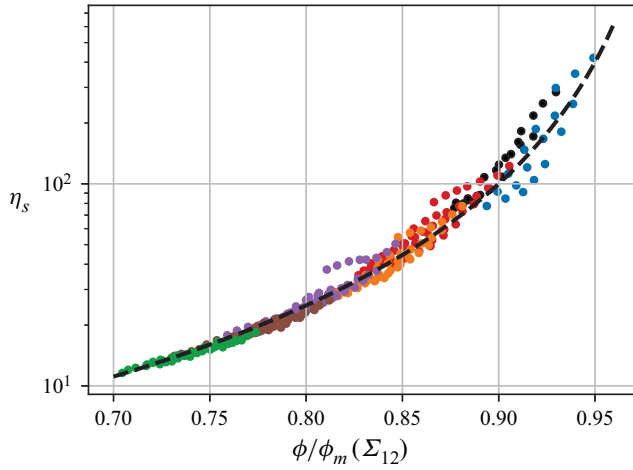
Figure 5. Relative viscosity η_s as function of $\phi/\phi_m(\Sigma_{12})$. Each symbol corresponds to the local measurement of the viscosity and of the particle volume fraction ϕ_m being deduced from the local shear stress value (4.6). Each colour labels $\bar{\Phi}$ values 0.520 (blue), 0.500 (black), 0.483 (red), 0.458 (orange), 0.435 (purple), 0.414 (brown), 0.394 (green). The black dashed line corresponds to the Maron–Pierce law: $\eta_s = (1 - \phi/\phi_m)^{-2}$.
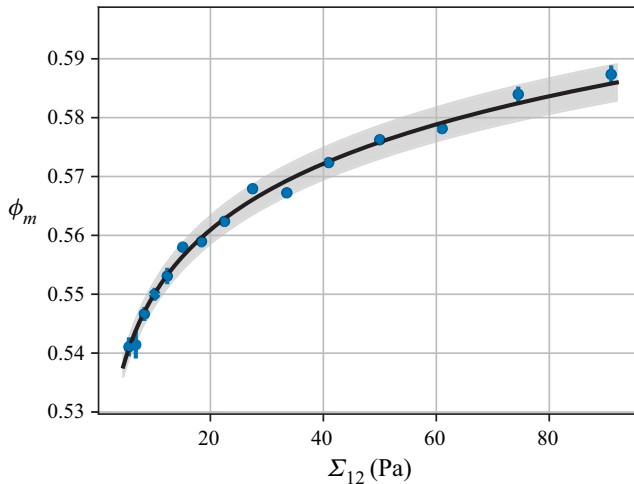

Figure 6. Jamming volume fraction ϕ_m as a function of the shear stress Σ_{12} deduced from figure 15. Black line: power-law fit, $\phi_m = 0.515\Sigma_{12}^{0.0286}$. Grey: confidence interval.

5. The characterization of Σ_{22}^p

Figure 3 displays the radial ϕ profiles measured for different values of the averaged volume fraction of suspension A. Outside the near wall regions, the particle volume fraction increases approximately linearly with r. In this section, we will make use of this outward particle migration to deduce Σ_{22}^p.

5.1. *Theoretical approach*

According to the SBM (Morris & Boulay 1999), in the absence of inertial effects, the steady particle concentration profile satisfies the balance of particle normal stresses:

$$\nabla \cdot \boldsymbol{\Sigma}^p = 0. \tag{5.1}$$

In the present study, as mentioned earlier, the flow Reynolds number is small. Nevertheless, rigorously speaking, (5.1) is valid only for the case of zero inertia. In the presence of inertial effects, obtaining a conservation equation for the particle phase is not trivial. However, Badia *et al.* (2022) showed recently that in the case where the relative velocity of the two phases may be neglected compared to the average velocity in all inertial terms, inertia can be accounted for by writing the equation

$$\nabla \cdot \boldsymbol{\Sigma}^p = -\phi(\rho_p - \rho_f)\left[\boldsymbol{g} - \frac{\mathrm{D}\boldsymbol{v}}{\mathrm{D}t}\right]. \tag{5.2}$$

Thus the inertial term is proportional to $(\rho_p - \rho_f)$ and can be neglected in such a way that (5.1) can be used.

Then in the velocity gradient direction, we obtain

$$\frac{1}{r}\frac{\partial(r\Sigma_{22}^p)}{\partial r} - \frac{\Sigma_{11}^p}{r} = 0, \tag{5.3}$$

which can be written as

$$\frac{\partial \Sigma_{22}^p}{\partial r} - \frac{N_1^p}{r} = 0, \tag{5.4}$$

where N_1^p is the first particle normal stress difference: $N_1^p = \Sigma_{11}^p - \Sigma_{22}^p$.

Following Morris & Boulay (1999), Σ_{22}^p can be rewritten as $\Sigma_{22}^p = -\lambda_2 \eta_0 \eta_n \dot{\gamma}$, with $\lambda_2 = \Sigma_{22}^p/\Sigma_{11}^p$ and $N_1^p = -\eta_0 \eta_n \dot{\gamma}(1 - \lambda_2)$, which gives

$$q_2(\phi, \phi_m) \equiv \frac{\eta_n(\phi, \phi_m)}{\eta_s(\phi, \phi_m)} = -\frac{\Sigma_{22}^p}{\Sigma_{12}}. \tag{5.5}$$

According to (4.2), this equation can be rewritten as

$$q_2(r) = \left(\frac{q_2(r_0)}{r_0^{(1+\lambda_2)/\lambda_2}}\right) \times r^{(1+\lambda_2)/\lambda_2} = Q_2(\Phi_0) \times r^{(1+\lambda_2)/\lambda_2}, \tag{5.6}$$

where r_0 is any radial position in the gap at which the particle volume fraction is equal to Φ_0.

The exact value of λ_2 is still debated. Nevertheless, several numerical studies (Gallier *et al.* 2014; Lobry *et al.* 2019) showed that $N_1^p \ll \Sigma_{12}$. In the case of frictional particles ($\mu \approx 0.5$), Gallier *et al.* (2014) showed $N_1^p/\Sigma_{12} \lesssim 10^{-2}$, while Σ_{22}^p is of the same order as Σ_{12} (Zarraga *et al.* 2000; Dbouk *et al.* 2013; Gallier *et al.* 2014), leading to $\lambda_2 \approx 1$. In the following, we will pursue the analysis with three values of λ_2, namely 0.8, 1 and 1.2, and we will show that the values of q_2 hardly vary with λ_2 (values between 0.8 and 1.2).

$$5.2. \text{ Determination of } q_2 = -\Sigma_{22}^p / \Sigma_{12}$$

In this subsection, we want to establish the variation of $q_2 = -\Sigma_{22}^p / \Sigma_{12}$ as a function of the ratio ϕ/ϕ_m. We compute $\phi_m(r)$ from $\Sigma_{12}(r)$ and (4.6) so that ϕ/ϕ_m is known for each radial position. However, it is essential to understand that, so far, we do not know the value Q_2 in (5.6), and the main issue is to find a way to determine it.

In order to obtain the value of Q_2, at a given position r_0 and for a given ratio $\phi(r_0)/\phi_m(r_0)$, we use the correlation proposed by Zarraga *et al.* (2000):

$$q_2(\phi/\phi_m) = -2.17 \times 0.62^3 (\phi/\phi_m)^3 \exp(2.34 \times 0.62(\phi/\phi_m)), \qquad (5.7)$$

where 0.62 is the jamming volume fraction obtained by Zarraga *et al.* (2000) for $\dot{\gamma} = 10 \, \text{s}^{-1}$. Although the suspensions studied by these authors present a noticeable shear-thinning behaviour, Zarraga *et al.* (2000) did not address how to introduce the shear-thinning behaviour into the constitutive laws that relate particle normal stresses to shear stress. We consider here that a possibility would be to write the constitutive laws as a function of ϕ/ϕ_m – rather than as a function of ϕ – because, since the shear viscosity has been shown to be a function of the sole ratio ϕ/ϕ_m (see § 4), writing the same for the particle normal stresses is the only way to keep a linear relation between Σ_{22}^p and Σ_{12}.

To set Q_2, we chose $r_0 \approx R_1 + 0.66 \times (R_2 - R_1)$, where the ratio ϕ/ϕ_m is the largest outside the layered regions (see the blue curve in figure 3 obtained for $\bar{\Phi} = 0.52$). At this position, $\phi/\phi_m = 0.93$ and (5.7) gives $Q_2 = 1.604$. This chosen reference point corresponds to the most extreme right point in figure 7. Now that the reference is set, (5.6) straightforwardly provides $q_2(\phi/\phi_m)$ for all the values of ϕ/ϕ_m obtained from the migration profile measured at $\bar{\Phi} = 0.52$ (the blue circles in figure 7). Next, we deal with the averaged concentration immediately smaller than 0.52, i.e. $\bar{\Phi} = 0.50$. For this new average concentration, the value of Q_2 is determined using the value of q_2 obtained with $\bar{\Phi} = 0.52$ over the overlap range of ϕ/ϕ_m. This enables us to plot the black circles in figure 7. We proceed in this same way for all the migration profiles measured at decreasing values of $\bar{\Phi}$ in order to build piece by piece the whole curve of figure 7. The coloured circles have been obtained by setting $\lambda_2 = 1$, while the two grey lines that delimit the grey zone correspond to the determination of q_2 with $\lambda = 0.8$ (lower curve) and $\lambda = 1.2$ (upper curve). Thus the choice of the exact value of λ_2 is not critical and affects the q_2 values.

We would also like to point out that all the results presented in figure 7 rely on the choice of the first value of Q_2 that we have used. Another choice of the value of Q_2 would have resulted in a curve with the same shape but shifted vertically. However, we are quite confident in our choice since the two most used correlations in the literature, those of Zarraga *et al.* (2000) (green line in figure 7) and Boyer *et al.* (2011) (black line in figure 7), give almost the same value of q_2 for the value of ϕ/ϕ_m chosen to set the reference.

In figure 7, the correlation proposed by Zarraga *et al.* (2000) (with $\phi_m = 0.62$) is also plotted, and rather good agreement with our results is observed even though there is a slight mismatch for the lowest values of ϕ/ϕ_m. On the contrary, the consistency between our results and the correlation proposed by Boyer *et al.* (2011) is less satisfactory, but we have to keep in mind that the work of Boyer *et al.* (2011) focuses mainly on very dense suspensions, as will be discussed in § 7.

6. The characterization of Σ_{33}^p

Here, we study the rheological behaviour of the negatively buoyant suspension B in order to determine the third particle normal stress Σ_{33}^p. This section may be considered as a
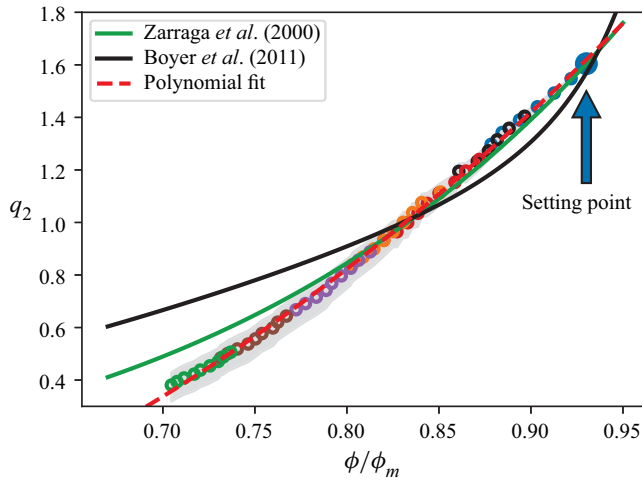
Figure 7. Variation of the function $q_2 = \eta_n/\eta_s = \Sigma_{22}^p/\Sigma_{12}$ with the ratio ϕ/ϕ_m. The colour code is the same as in figure 15, for average concentration $\bar{\Phi}$ values 0.520 (blue), 0.500 (black), 0.483 (red), 0.458 (orange), 0.435 (purple), 0.414 (brown), and 0.394 (green). Green solid line: correlation of Zarraga *et al.* (2000) ($\phi_m = 0.62$). The two grey lines that delimit the grey zone correspond to the determination of q_2 with $\lambda = 0.8$ (lower curve) and $\lambda = 1.2$ (upper curve). Black solid line: correlation of Boyer *et al.* (2011) ($\phi_m = 0.585$). Red dashed line: polynomial fit $q_2 = 5.47(\phi/\phi_m)^2 - 3.35(\phi/\phi_m)$.

next step of our previous work on viscous resuspension (d'Ambrosio *et al.* 2021), where we determined Σ_{33}^p from the local measurements of $\phi(z)$ by solving the particle stress balance in the vertical direction. We start from the z projection of the total stress balance:

$$\frac{1}{r}\frac{\partial (r\Sigma_{23})}{\partial r} + \frac{\partial \Sigma_{33}}{\partial z} = \Delta\rho\, g\phi. \tag{6.1}$$

We first showed, thanks to the analysis of the velocity profiles measured in the resuspension experiments, that the first left-hand-side term can be neglected, leading to the following simple equation for the third particle normal stress (see supplementary material of d'Ambrosio *et al.* 2021):

$$\frac{\partial \Sigma_{33}^p}{\partial z} = \Delta\rho\, g\phi, \tag{6.2}$$

with the boundary condition $\Sigma_{33}^p = 0$ for $z = h$, where h denotes the height of the interface between the resuspended layer and the clear fluid. Besides, we derived the local shear rate $\dot{\gamma}(r, z)$ from the measurement of the azimuthal velocity field $v_\theta(r, z)$. In agreement with the work of Saint-Michel *et al.* (2019), we highlighted the nonlinear variation of Σ_{33}^p with $\dot{\gamma}$:

$$\frac{\Sigma_{33}^p}{\eta_0\dot{\gamma}^n} = f(\phi), \quad \text{with } n = 0.7. \tag{6.3}$$

This nonlinear behaviour raises questions. On the one hand, it is anticipated that Σ_{33}^p does not vary linearly with $\dot{\gamma}$ since it is expected to be proportional to the shear stress, which itself may not vary linearly with shear rate (see, for instance, Tanner (2018) or Zarraga *et al.* (2000) and Appendix B). But on the other hand, the exponent in the shear stress versus shear rate relation is all but constant and decreases when the particle fraction increases (see

967 A34-16

Appendix B), which disagrees with (6.3). In this section, we will show that the relation between Σ_{33}^p and Σ_{12} is linear, and that $\Sigma_{33}^p/(\eta_0\dot{\gamma})$ is a function of only ϕ/ϕ_m.

6.1. *Determination of the shear stress field in viscous resuspension experiments*

As mentioned earlier, the shear stress cannot be deduced from the torque applied to the rotor since the particle volume fraction varies along the z direction, which precludes the assumption that the stress is vertically homogeneous. To determine $\Sigma_{12}(r, z)$, we make the hypothesis that suspensions A and B obey the same constitutive laws (see § 4.2):

$$\eta_s(\phi, \phi_m) = (1 - \phi/\phi_m)^{-2} \quad \text{and} \quad \phi_m = 0.515\,\Sigma_{12}^{0.0286}. \tag{6.4a,b}$$

Thus from the local measurement of $\phi(r, z)$ and $\dot{\gamma}(r, z)$, the local shear stress $\Sigma_{12}(r, z)$ can be deduced from (6.4a,b) and the implicit equation

$$\Sigma_{12}(r, z) = \eta_s(\phi(r, z), \phi_m(\Sigma_{12})) \times \dot{\gamma}(r, z). \tag{6.5}$$

Using this equation is possible because, as shown in the supplementary material of d'Ambrosio *et al.* (2021), the 13-component of the rate of deformation tensor is very small compared to the 12-component. The local jamming volume fraction $\phi_m(r, z)$ is then determined from $\Sigma_{12}(r, z)$.

Note that assuming that suspensions A and B obey the same constitutive law (6.4a,b) is a rather strong hypothesis that is difficult to justify *a priori*. However, the facts that the particles are exactly the same for both suspensions and that the suspending fluids are quite similar (both based on water/Triton X-100 mixtures) make this hypothesis quite reasonable. Moreover, we will see in the next two subsections that the use of this assumption provides consistent results, in agreement with the literature with, in particular, the linear variation of Σ_{33}^p with Σ_{12} and the measurement of the ratio $\Sigma_{33}^p/\Sigma_{22}^p \approx 0.5$.

6.2. *Variation of Σ_{33}^p with Σ_{12}*

Figure 8 displays the variation of the third particle normal stress $-\Sigma_{33}^p$ with the shear stress Σ_{12} for different values of ϕ/ϕ_m, targeted across all the different experiments of viscous resuspension done with suspension B. Although the data dispersion is rather large, we observe that a linear relation exists between Σ_{33}^p and Σ_{12}, in agreement with the literature (Guazzelli & Pouliquen 2018).

6.3. *Shear-thinning behaviour of Σ_{33}^p*

In figure 9(*a*), we have reproduced the variation of $-\Sigma_{33}^p/\eta_0\dot{\gamma}$ with ϕ, already displayed in our previous paper (d'Ambrosio *et al.* 2021). The colour scale indicates the value of Σ_{12} for each point, deduced from (6.4a,b) and (6.5). We observe that for a given value of $-\Sigma_{33}^p/\eta_0\dot{\gamma}$, the shear stress tends to increase as ϕ rises. This observation suggests that the thickness of the curve is not due to experimental noise but rather, the particle volume fraction is not the only variable controlling the value of the ratio $-\Sigma_{33}^p/\eta_0\dot{\gamma}$. The dispersion of the data is reduced significantly when this ratio is plotted against ϕ/ϕ_m, where ϕ_m is a function of the shear stress, as shown in figure 9(*b*). This observation is consistent with the linear variation of Σ_{33}^p with Σ_{12} presented in the previous subsection together with the shear-thinning behaviour of the suspension, and provides a plausible physical explanation for the nonlinear behaviour of Σ_{33}^p with $\dot{\gamma}$
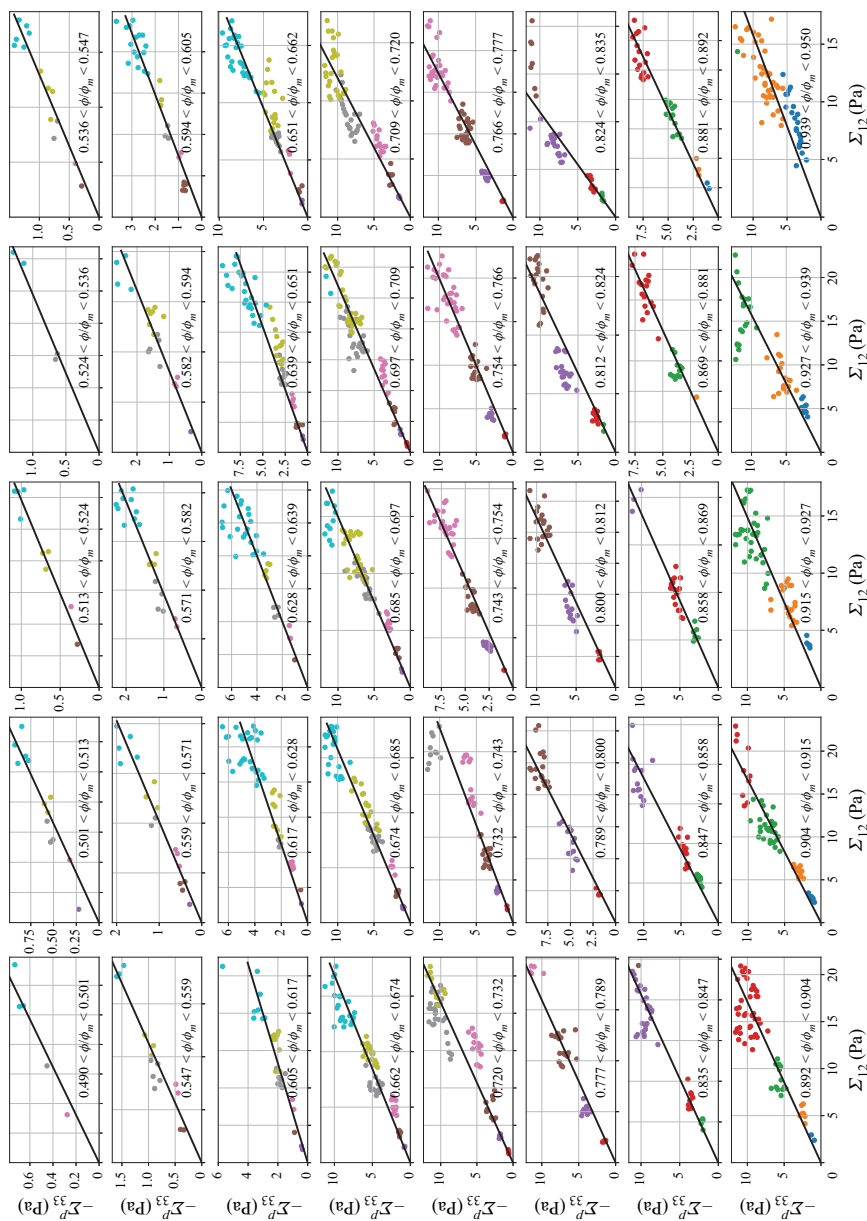
Figure 8. Variation of the third particle normal stress $-\Sigma_{33}^p$ with the shear stress Σ_{12} for different values of ϕ/ϕ_m. Black lines: linear fits. Each symbol colour corresponds to a resuspension experiment performed with a given angular velocity of the rotor, Ω: 0.3 rpm (blue), 0.5 rpm (orange), 1 rpm (green), 2 rpm (red), 5 rpm (purple), 10 rpm (brown), 20 rpm (pink), 30 rpm (gray), 40 rpm (olive), 60 rpm (cyan).

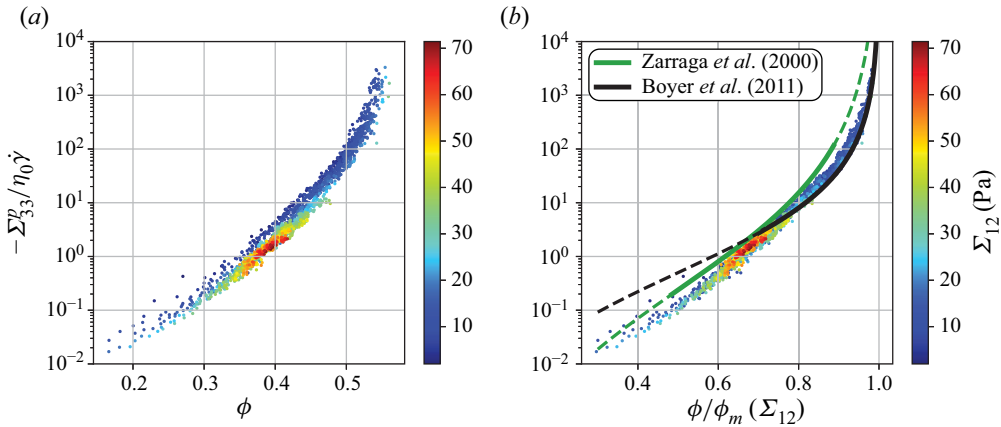Figure 9. Variation of the ratio $-\Sigma_{33}^p/\eta_0\dot{\gamma}$ as a function of (*a*) ϕ and (*b*) of ϕ/ϕ_m. The colour bars display the values of the shear stress calculated from (6.4*a,b*) and (6.5). The correlation of Zarraga *et al.* (2000) with $\phi_m = 0.62$ is also plotted (green line) as well as the results of Boyer *et al.* (2011) with $\phi_m = 0.585$, considering $\Sigma_{33}^p/\Sigma_{22}^p = 0.5$ (black line). The solid lines show the domains where these laws have been determined experimentally, while the dashed lines correspond to extrapolations of the data.

recorded by both Saint-Michel *et al.* (2019) and d'Ambrosio *et al.* (2021), as discussed in the introduction of § 6.

In figure 9(*b*), the correlations proposed by Boyer *et al.* (2011) (black solid line) and Zarraga *et al.* (2000) (green solid line) are also plotted. It is observed that our results are in good agreement with each of these two correlations in the domains of ϕ/ϕ_m in which they have been originally determined: $\phi/\phi_m \in [0.48, 0.89]$ for Zarraga *et al.* (2000), and $\phi/\phi_m \in [0.7, 0.999]$ for Boyer *et al.* (2011). But neither the law proposed by Boyer *et al.* (2011) nor the one proposed by Zarraga *et al.* (2000) is valid on the whole range of values of ϕ/ϕ_m explored in the present study. This point will be discussed again in § 7.

To conclude, the shear rate dependence of Σ_{33}^p can be captured by the variation of the jamming fraction with the shear stress, as is done frequently for the shear viscosity. We have shown that Σ_{33}^p is proportional to Σ_{12}, which provides a satisfactory physical explanation for the nonlinear variation of Σ_{33}^p with $\dot{\gamma}$ observed by Saint-Michel *et al.* (2019) and d'Ambrosio *et al.* (2021).

7. $\mu(J)$ rheology

Our results obtained with both suspensions A and B can be used to write the constitutive laws $\mu = \Sigma_{12}/\Sigma_{22}^p$ and ϕ/ϕ_m as a function of $J = \eta_0\dot{\gamma}/\Sigma_{22}^p$, in the frame of the $\mu(J)$ rheology proposed by Boyer *et al.* (2011). It is straightforward to deduce these constitutive laws from the determination of Σ_{22}^p obtained from the measurement of the radial profile of particle volume fraction carried on the neutrally buoyant suspension, together with the measurement of the local shear rate.

In addition, the viscous resuspension experiments carried out on suspension B can be used. In figure 10, the ratio $\lambda_{32} = \Sigma_{33}^p/\Sigma_{22}^p = \Sigma_{33}^p/q_2\Sigma_{12}$ is plotted as a function of ϕ/ϕ_m in the range where q_2 has been measured ($\phi/\phi_m \in [0.7, 0.95]$; see figure 7). The quite wide scattering of the data is likely related to the limited accuracy of the measurement of Σ_{33}^p as a function of the ratio ϕ/ϕ_m, already observed in figure 9(*b*). It should also be noted that
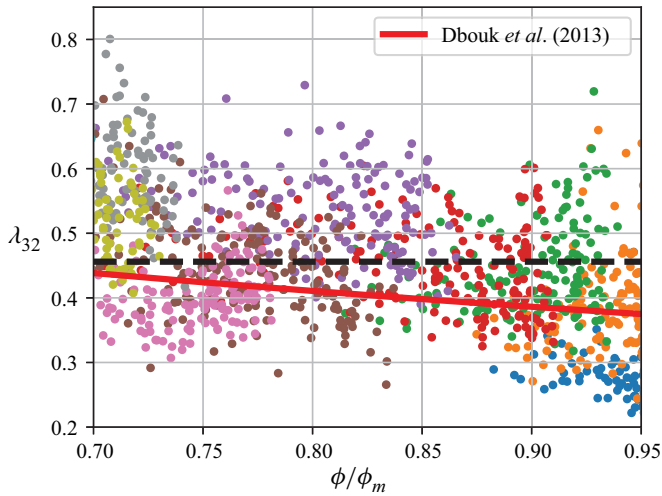
Figure 10. Variation of the coefficient $\lambda_{32} = \Sigma_{33}^p/\Sigma_{22}^p = \lambda_3/\lambda_2$ against the ratio ϕ/ϕ_m. The red line shows the Dbouk *et al.* (2013) result: $\lambda_{32} = (-0.0153\phi_m \times \phi/\phi_m + 0.547)/(1.4\phi_m \times \phi/\phi_m + 0.665)$, with $\phi_m = 0.58$. The black dashed line indicates the averaged value of $\lambda_{32} = 0.456$. Each symbol colour corresponds to a resuspension experiment at a given angular velocity of the rotor, i.e. Ω values 0.3 rpm (blue), 0.5 rpm (orange), 1 rpm (green), 2 rpm (red), 5 rpm (purple), 10 rpm (brown), 20 rpm (pink), 30 rpm (gray), 40 rpm (olive).

in these two figures, all of the data points are reported without any averaging, which also contributes to the scattering. Despite the data dispersion, the good thing is that the typical value measured for the ratio λ_{32} is close to the values found in the literature. In the original SBM (Morris & Boulay 1999), this ratio is approximated by a constant that is independent of the particle volume fraction and approximately equal to 0.6 (the ratio of $\lambda_3 \approx 0.5$ over $\lambda_2 \approx 0.8$ in the SBM). Note that in the present study, we have set $\lambda_2 = 1$, which would lead to $\lambda_{32} \approx 0.5$. Even though the scatter of the data in figure 10 is rather large, it is quite satisfactory that λ_{32} hardly varies with ϕ/ϕ_m, that the slight decrease is very similar to what has been measured by Dbouk *et al.* (2013) and that the average measured value is 0.456, in rather good agreement with what was expected. It has also to be noted that this value is very close to the result reported by Zarraga *et al.* (2000), who have found $\Sigma_{33}^p/\Sigma_{22}^p = 0.46$.

In the following, we will use $\lambda_{32} = 0.456$ to deduce J and μ from the resuspension experiments:

$$\mu = \lambda_{32} \times \Sigma_{12}/\Sigma_{33}^p \quad \text{and} \quad J = \lambda_{32} \times \eta_0\dot{\gamma}/\Sigma_{33}^p. \tag{7.1a,b}$$

The variations of $(1 - \phi/\phi_m)$ and μ with J are plotted in figures 11(*a*) and 11(*b*), respectively. The thick black line corresponds to the results obtained from the measurement of the radial profile in the neutrally buoyant suspension, while the coloured circles have been deduced from the resuspension experiments. First, note that figure 11(*a*) does not provide any new information since it is strictly equivalent to what was plotted in figure 9(*b*). Second, it should be mentioned that the uncertainty on the measurements obtained for $J \lesssim 10^{-3} - 10^{-2}$ is quite large since the uncertainty on both ϕ and ϕ_m is of the order of 1 %, which leads to an absolute error on $(1 - \phi/\phi_m)$ of the order of 10^{-2}. Nevertheless, the present results are rather consistent with the results of Boyer *et al.* (2011), Tapia *et al.* (2019) and Etcheverry (2022) (respectively, the green, purple and dark teal curves in figures 11(*a*) and 11(*b*)), who observed a variation of $(1 - \phi/\phi_m)$ in $J^{1/2}$ for
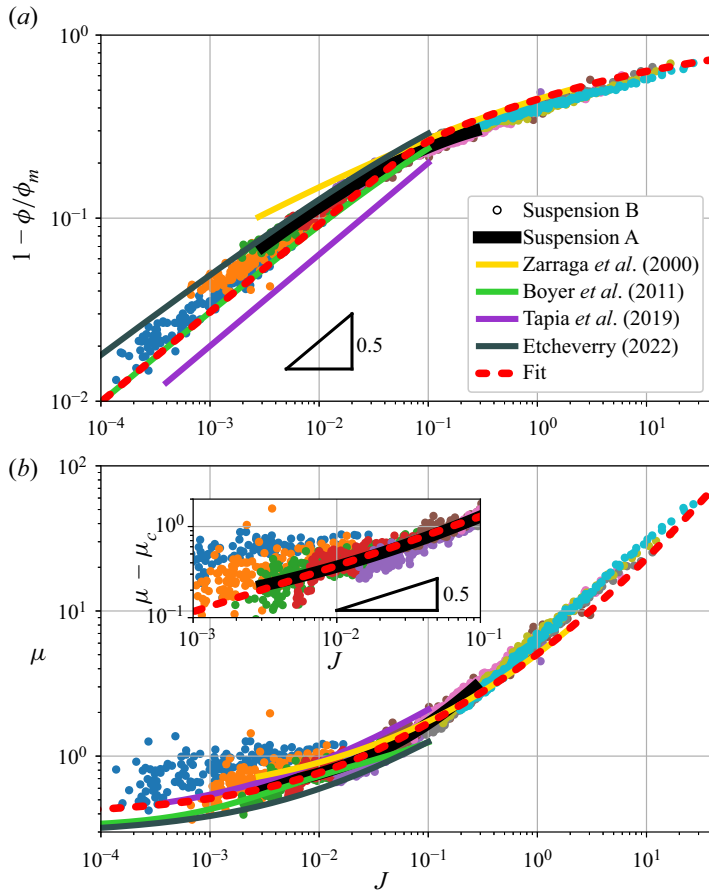
967 A34-20

Figure 11. (*a*) Variation of $(1 - \phi/\phi_m)$ with J. (*b*) Variation of μ with J. The thick black line corresponds to the results extracted from the radial migration profiles (suspension A). The coloured circles correspond to the results obtained through the study of the viscous resuspension (suspension B) for various angular velocities (same colour code as in figure 10). The yellow, green, purple and dark teal lines correspond to the results obtained by Zarraga *et al.* (2000), Boyer *et al.* (2011), Tapia *et al.* (2019) and Etcheverry (2022), respectively. Our data show clear agreement with the results of Boyer *et al.* (2011) for $J < O(10^{-1})$, and with those of Zarraga *et al.* (2000) for $J > O(10^{-1})$. The rheological behaviour over the whole range of investigated viscous numbers is captured by introducing a smooth transition function that interpolates between the law proposed by Boyer *et al.* (2011) and that obtained by Zarraga *et al.* (2000) (see (7.2) and (7.7)). The value $J_c = 6 \times 10^{-2}$ is given by the best fit of (7.2) to the experimental variation of $(1 - \phi/\phi_m)$ with J (red dashed line in (*a*)). The fitting of Boyer's correlation to the variation of μ with J deduced from the radial migration profiles (suspension A) for $J \in [3 \times 10^{-3}, J_c]$ yields $\mu_c = 0.39$ and $A_\mu = 3.7$. The best fit is shown in the inset of (*b*). The red dashed line in (*b*) is the result of (7.7) with $J_c = 6 \times 10^{-2}$, $A_\mu = 3.7$ and $\mu_c = 0.39$.

$J < 10^{-1}$. For higher values of J, the variation of $(1 - \phi/\phi_m)$ with J deviates from the above scaling, and our results show very good agreement with those of Zarraga *et al.* (2000) (yellow solid curve). Note that this observation is completely equivalent to the one that we made when discussing the graph in figure 9(*b*).

Hence the variation of $1 - \phi/\phi_m$ as a function of J that has been obtained from the measurements of the vertical concentration profiles in the resuspension experiments seems to be able to bridge the gap between the scalings proposed by Boyer *et al.* (2011) for

$J \lesssim 10^{-1}$ on the one hand, and by Zarraga *et al.* (2000) for $J \gtrsim 10^{-1}$ on the other hand. Our results on the whole range of investigated viscous numbers ($10^{-4} < J < 30$) are well fitted by introducing a smooth transition function $\mathcal{T}(J/J_c)$ that interpolates between the law proposed by Boyer *et al.* (2011) ($\mathcal{B}_\phi(J)$ hereafter), and that obtained by Zarraga *et al.* (2000) ($\mathcal{Z}_\phi(J)$ hereafter):

$$1 - \frac{\phi}{\phi_m} = \mathcal{T}\left(\frac{J}{J_c}\right)\mathcal{B}_\phi(J) + \left(1 - \mathcal{T}\left(\frac{J}{J_c}\right)\right)\mathcal{Z}_\phi(J), \tag{7.2}$$

where

$$\mathcal{T}(x) = \frac{1}{2}\left(1 + \frac{1 - x^2}{1 + x^2}\right), \tag{7.3}$$

$$\mathcal{B}_\phi(J) = 1 - \frac{1}{1 + J^{1/2}}, \tag{7.4}$$

$$\mathcal{Z}_\phi(J) = \frac{J^{1/3}}{A_z + J^{1/3}}, \quad \text{with } A_z \approx 1.25, \tag{7.5}$$

where $\mathcal{Z}_\phi$ is deduced from the correlations proposed by Zarraga *et al.* (2000) to relate Σ_{22}^p to Σ_{12}, and η_s to ϕ, together with the definition of the viscous number $J = \eta_0\dot{\gamma}/\Sigma_{22}^p = (1/\eta_s)(\Sigma_{12}/\Sigma_{22}^p)$.

The red dashed line in figure 11(*a*) shows the result of the best fit, which yields $J_c = 6 \times 10^{-2}$, a value close to the quite abrupt change of slope observed in figure 11(*a*).

Our data on the variation of μ with J are plotted in figure 11(*b*) together with the results of Zarraga *et al.* (2000) in the range $J \in [3 \times 10^{-3}, 2]$ (yellow solid line) and the results of Boyer *et al.* (2011) (green line), Tapia *et al.* (2019) (purple line) and Etcheverry (2022) (dark teal line) obtained with $J < 10^{-1}$. Our results are consistent with those of Zarraga *et al.* (2000) and in a rather good agreement with those of Boyer *et al.* (2011) and Tapia *et al.* (2019) for small values of J, even though we measured slightly higher effective friction coefficients for the smallest J values. Before going further, it is necessary to recall that the measurements at small J values suffer from a large uncertainty: the uncertainty evaluated on the ratio ϕ/ϕ_m is $O(10^{-2})$, which results in a relative uncertainty of more than 50 % on the evaluation of the shear stress for $(1 - \phi/\phi_m) \approx 0.04$, i.e. $J \approx 10^{-3}$. To this, must be added the uncertainty on Σ_{33}^p that is likely to be of the same order of magnitude. The uncertainty on the values of μ determined from the radial migration profiles measured in suspension A is much smaller. That is why we decided to determine the law $\mu(J)$ on the basis of these last results obtained for $J > 3 \times 10^{-3}$.

We fit our results obtained with suspension A (black thick curve in figure 11*b*) in the range $J \in [3 \times 10^{-3}, J_c]$ to the correlation proposed by Boyer *et al.* (2011) in the limit of small J (DeGiuli *et al.* 2015; Trulsson, DeGiuli & Wyart 2017; Tapia *et al.* 2019) in order to reduce the number of free parameters:

$$\mathcal{B}_\mu(J) = \mu_c + A_\mu J^{1/2}. \tag{7.6}$$

The best fit of our data yields $A_\mu = 3.7$ and $\mu_c = 0.39$. This value of μ_c is slightly higher but not significantly different from the values given by Boyer *et al.* (2011) and Tapia *et al.* (2019), i.e. $\mu_c = 0.32$ and 0.37, respectively. Furthermore, the inset of figure 11(*b*) shows that taking $\mu_c = 0.39$ enables us to obtain the expected behaviour, $\mu - \mu_c \propto J^{1/2}$, as well for the neutrally buoyant suspension (black line) as for the non-neutrally

967 A34-22

buoyant one (circles) for $J \lesssim 10^{-1}$. The value of A_μ is between the value measured by Boyer *et al.* (2011), 1.46, and the value measured by Tapia *et al.* (2019), 5.45 and comparable to the values reported by Dagois-Bohy *et al.* (2015), $A_\mu = 4.0$, and recently by Etcheverry (2022), $A_\mu = 3.05$.

Finally, the variation $\mu(J)$ measured over the whole range of viscous numbers can again be represented by using the same smooth transition function $\mathcal{T}(J/J_c)$ that was employed previously to capture the variation of $1 - \phi/\phi_m$ with J (see (7.3)):

$$\mu = \mathcal{T}\left(\frac{J}{J_c}\right)\mathcal{B}_\mu(J) + \left(1 - \mathcal{T}\left(\frac{J}{J_c}\right)\right)\mathcal{Z}_\mu(J), \qquad (7.7)$$

where the value of J_c is kept the same: $J_c = 6 \times 10^{-2}$. Here, $\mathcal{B}_\mu$ is given by (7.6), and $\mathcal{Z}_\mu$ is the variation of μ with J deduced from the correlation proposed by Zarraga *et al.* (2000) together with (7.5):

$$\mathcal{Z}_\mu(J) = \frac{1}{2.17\phi^3\,\mathrm{e}^{2.34\phi}}, \quad \text{with } \phi = \frac{0.62}{1 + 0.62(J/0.46)^{1/3}}. \qquad (7.8)$$

This result is displayed in figure 11(*b*) by the red dashed line.

To conclude this section, we have obtained results, whether for the variation of $1 - \phi/\phi_m$ or of μ with J, that are consistent with those of Boyer *et al.* (2011) for the low values of J, and with those of Zarraga *et al.* (2000) for higher values of J, and we have shown that the transition between these two behaviours observed by Boyer *et al.* (2011) on the one hand and Zarraga *et al.* (2000) on the other hand took place for a viscous number of approximately 6×10^{-2}.

8. Concluding remarks

In this paper, two different monodisperse suspensions made of the same spherical particles suspended in viscous Newtonian liquids have been sheared in a wide-gap cylindrical Couette cell in order to study and characterize their rheological behaviour. The shear viscosity as well as the second and third particle normal stresses have been measured, providing the constitutive laws in the $\mu(J)$ framework over a large range of viscous numbers.

The first suspension is neutrally buoyant, while the liquid in the second is less dense than the particles. For both suspensions, we conducted local measurements of both the velocity and the solid volume fraction by optical imaging, as already done in a previous work for the negatively buoyant suspension (d'Ambrosio *et al.* 2021). In both suspensions, we observed a strong layering of the particles near the walls. As a consequence, only the measurements outside these structured zones have been considered to compute the different rheological constitutive laws.

We measured the viscosity of the neutrally buoyant suspension and observed a moderate but effective shear-thinning behaviour that can be captured by the variation of the jamming fraction with the shear stress. The measurements of the radial profile of particle volume fraction gave access to the second particle normal stress Σ_{22}^p. The variation of the ratio $q_2 = \Sigma_{22}^p/\Sigma_{12}$ is determined over the range $\phi/\phi_m \in [0.70, 0.93]$. We found good agreement with the results of Zarraga *et al.* (2000), even though a slight discrepancy occurs at low ϕ/ϕ_m ($\phi/\phi_m \lesssim 0.8$).

E. d'Ambrosio, F. Blanc and E. Lemaire

The second part of the paper focuses on the negatively buoyant suspension. We use the rheological laws $\eta_s(\phi/\phi_m)$ and $\phi_m(\Sigma_{12})$ established for the density-matched suspension to pursue and complete our previous study on the viscous resuspension (d'Ambrosio *et al.* 2021). We first show that Σ_{33}^p is proportional to Σ_{12}. This result is quite important, in particular because it provides a physically meaningful explanation for the nonlinear variation of Σ_{33}^p with $\dot{\gamma}$, measured by both Saint-Michel *et al.* (2019) and d'Ambrosio *et al.* (2021). The ratio $\Sigma_{33}^p/\eta_0\dot{\gamma}$ is shown to be a function of ϕ/ϕ_m – instead of ϕ – where ϕ_m is a function of Σ_{12}. Interestingly, our results show very good agreement on the one hand with those reported by Boyer *et al.* (2011) for high volume fractions and on the other hand with those of Zarraga *et al.* (2000) obtained for lower particle fractions. The main value of our results is that they have been obtained over a range of ϕ/ϕ_m values ($0.3 \lesssim \phi/\phi_m \lesssim 0.98$) that allows for exploration of both the domain of moderate volume fraction studied by Zarraga *et al.* (2000) ($0.5 \lesssim \phi/\phi_m \lesssim 0.9$) and the very dense regime studied by Boyer *et al.* (2011) ($10^{-3} \lesssim \phi_m - \phi \lesssim 10^{-1}$). Our results thus seem to confirm the results obtained by these two groups, although the correlations proposed by the authors are very different from each other. This leads to the first conclusion that the constitutive laws proposed by Zarraga *et al.* (2000) on the one hand and by Boyer *et al.* (2011) on the other hand are effective in the domains on which they have been established experimentally but cannot be extrapolated outside these domains.

This outcome is even more obvious when the rheological behaviour is described in the framework of the $\mu(J)$ rheology. The decades of viscous numbers that have been covered ($2 \times 10^{-4} < J < 30$) offer the possibility to cross from concentrated regimes ($1 - \phi/\phi_m \approx 10^{-2}$) to semi-dilute regimes ($1 - \phi/\phi_m \approx 7 \times 10^{-1}$). Note that the characterization of the rheology over this large range of viscous numbers has been possible only thanks to the analysis of the resuspension experiments. The range of viscous numbers accessible through the radial migration experiments is much narrower ($3 \times 10^{-3} < J < 3 \times 10^{-1}$). However, these latter experiments have several advantages. They provide more accurate results than the resuspension experiments, for rather small viscous numbers. The comparison of the results obtained with the two kinds of suspensions shows very good agreement and thus provides *a posteriori* validation of the data.

Our results show clearly that the correlation proposed by Boyer *et al.* (2011) accounts adequately for the rheological behaviour in the small viscous number (or large volume fraction) range, while the laws provided by Zarraga *et al.* (2000) are well suited to describe the rheology measured at large viscous numbers. The transition between the two regimes occurs for a viscous number of the order of 6×10^{-2}. Finally, the variation of both ϕ/ϕ_m and μ with J over the full range of investigated viscous numbers can be captured by introducing a smooth transition function that interpolates between the law proposed by Boyer *et al.* (2011) and that obtained by Zarraga *et al.* (2000).

Declaration of interests. The authors report no conflict of interest.

Author ORCIDs.

Ⓓ Enzo d'Ambrosio https://orcid.org/0000-0002-4499-3580;

Ⓓ Elisabeth Lemaire https://orcid.org/0000-0001-8609-2783.

967 A34-24

Appendix A. Velocity profiles in the neutrally buoyant suspension

Figure 12 displays the radial variation of the relative velocity $v_\theta/(\Omega R_1)$ for the different average volume fractions and for each rotor angular velocity value. As the average particle volume fraction is increased, the apparent wall slip of the suspension is enhanced.
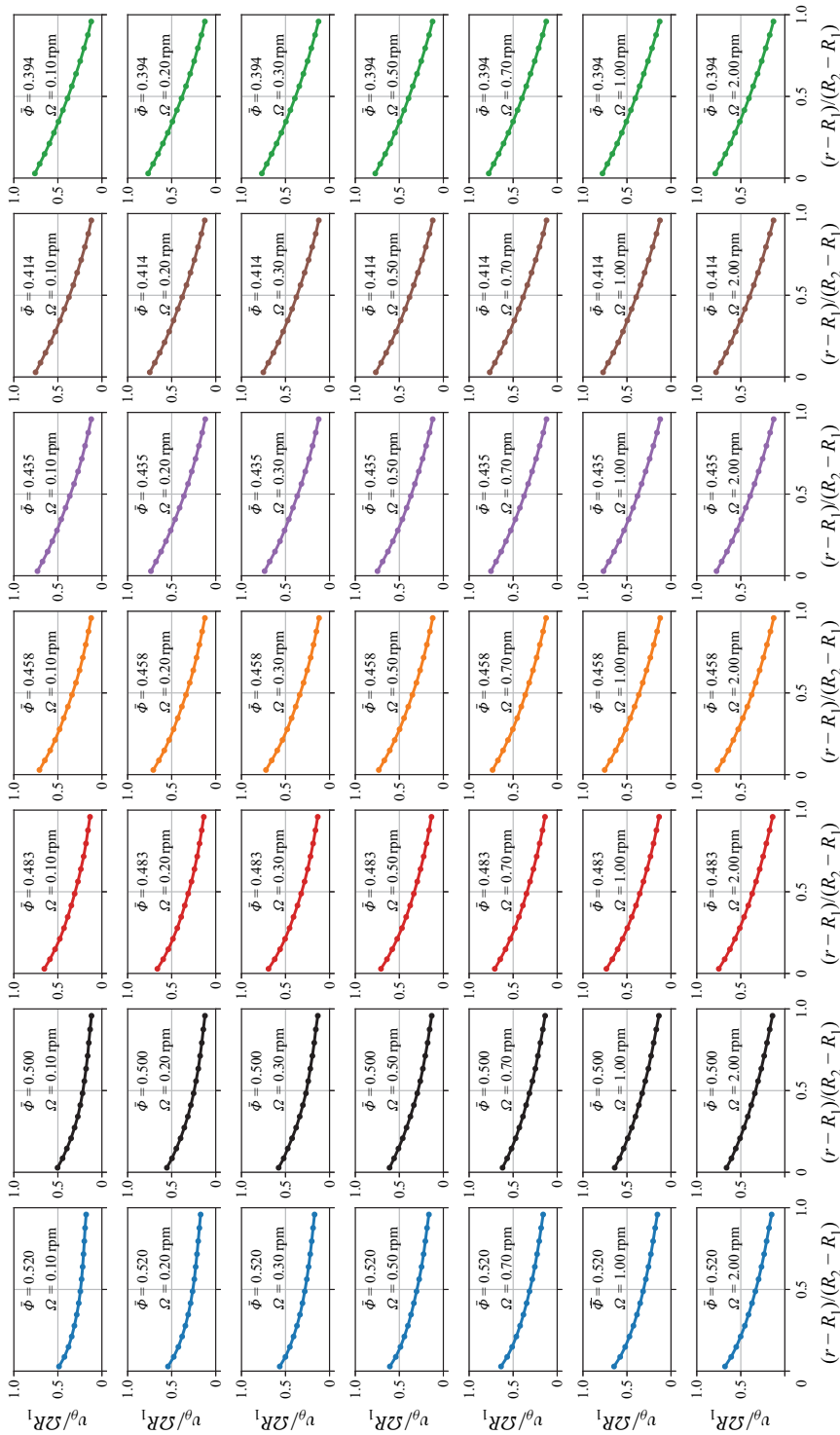
Figure 12. Steady radial profiles of the relative velocity $v_\theta/\Omega R_1$ for the different average volume fractions $\bar{\Phi}$ and for each rotor angular velocity value Ω.

Appendix B. Shear-thinning behaviour modelled by Herschel–Bulkley laws

Flow curves of shear-thinning suspensions are often fitted by a Herschel–Bulkley law (Coussot & Piau 1994; Schatzmann *et al.* 2003; Sosio & Crosta 2009; Mueller *et al.* 2010; Vance *et al.* 2015):

$$\Sigma_{12} = \tau_c + K\dot{\gamma}^{\nu}, \tag{B1}$$

where the consistency, the yield stress and the shear-thinning index, respectively denoted by K, τ_c and ν, are expected to be functions of the particle fraction ϕ. Figure 13 displays the variation of the shear stress Σ_{12} with the shear rate $\dot{\gamma}$ for different local particle volume fractions together with Herschel–Bulkley fits. The variation of these three parameters with ϕ is depicted in figure 14. As expected, the behaviour of the suspension is almost Newtonian for the smallest concentrations ($\nu > 0.9$ for $\phi < 0.45$), and becomes more and more shear-thinning as the volume fraction is raised: the exponent decreases while the consistency and the yield stress increase with ϕ.
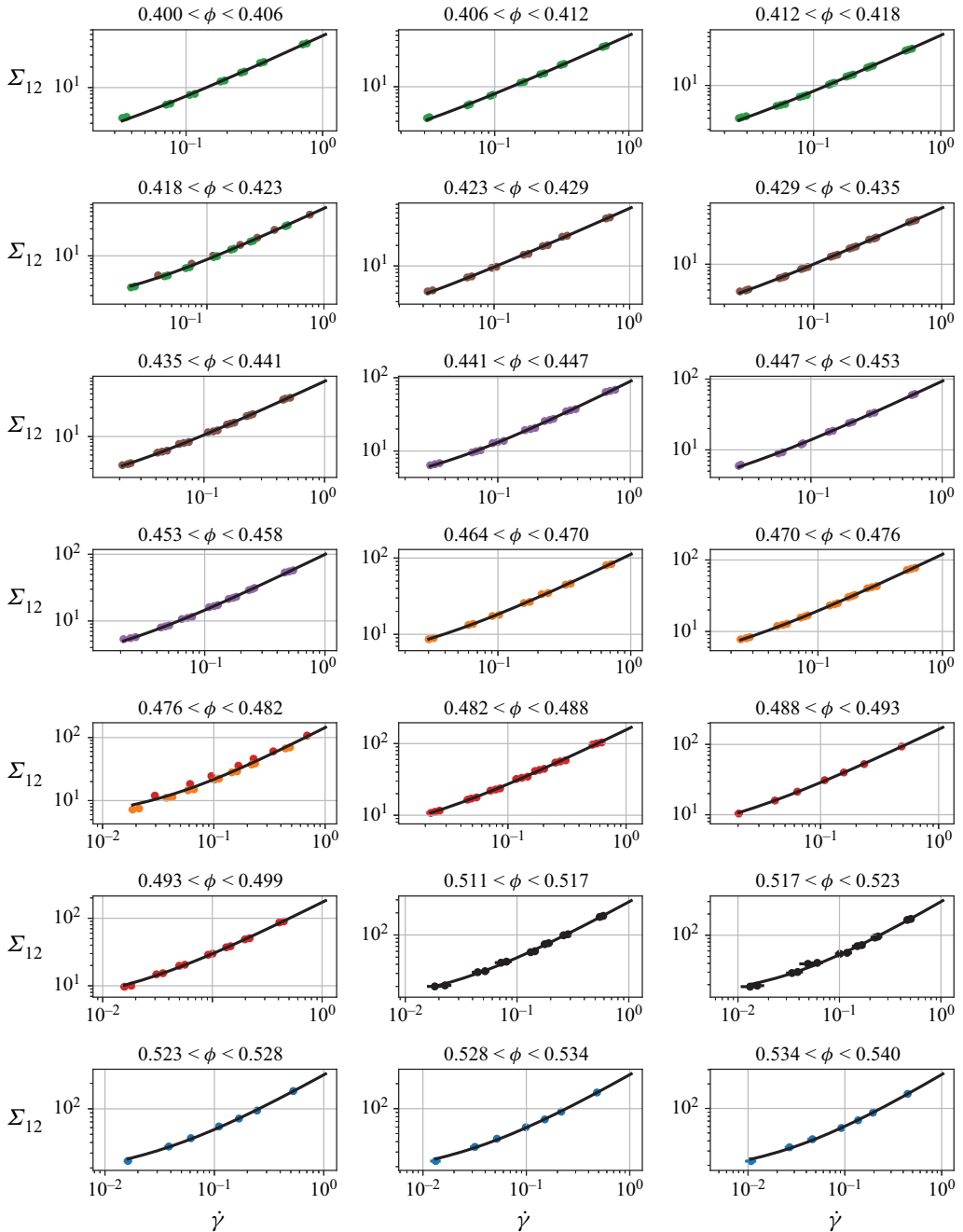
Figure 13. Variation of the local shear stress Σ_{12} with the local shear rate $\dot{\gamma}$. Each curve is obtained by selecting among all the 49 experiments ($7\Omega \times 7\bar{\Phi}$) the radial positions where the particle volume fraction is in the range indicated above each plot. Each colour labels $\bar{\Phi}$ values 0.52 (blue), 0.50 (black), 0.483 (red), 0.458 (orange), 0.435 (purple), 0.414 (green). Black line: Herschel–Bulkley fit (see (B1)).
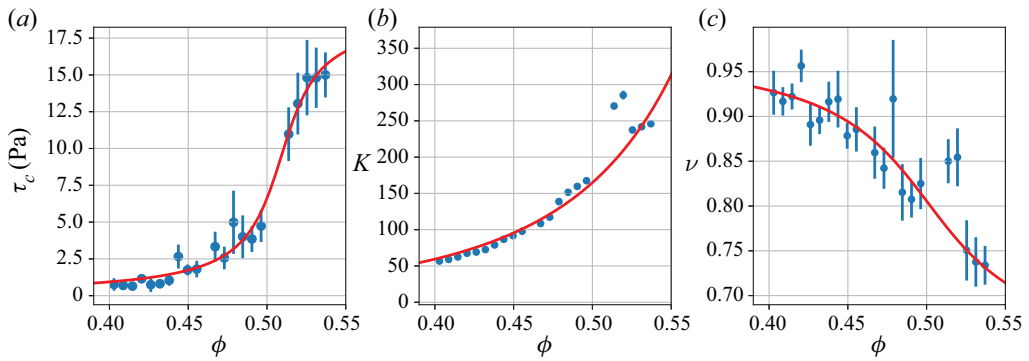
Figure 14. Parameters of the Herschel–Bulkley law as functions of the volume fraction ϕ. Here, τ_c is the yield stress, K is the consistency index, and ν is the shear-thinning index.

Appendix C. Fitting of the Maron–Pierce law to the experimental data

Figure 15 shows the variation of $1/\sqrt{\eta_S}$ with ϕ for different values of the local shear stress, measured for suspension A.
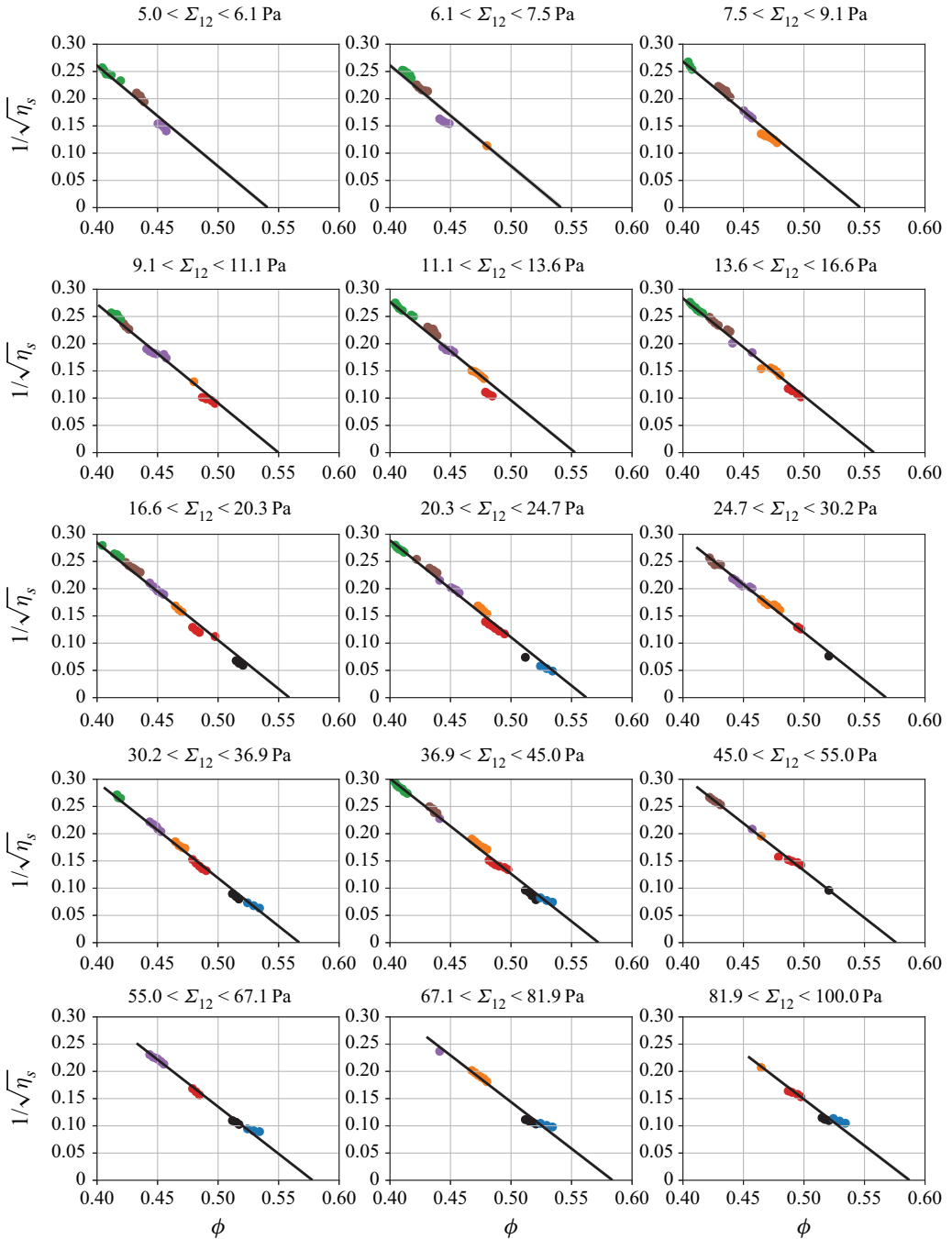
Figure 15. Variation of $1/\sqrt{\eta_s}$ with the volume fraction ϕ measured locally for different given shear stress values. Each curve is obtained by selecting among all the 49 experiments ($7\Omega \times 7\bar{\Phi}$) the radial positions where the shear stress is in the range indicated above each plot. Each colour labels $\bar{\Phi}$ values 0.52 (blue), 0.50 (black), 0.483 (red), 0.458 (orange), 0.435 (purple), 0.414 (green). Black line: linear fittings by $1/\sqrt{\eta_s} = 1 - \phi/\phi_m$.

References

ABBOTT, J.R., TETLOW, N., GRAHAM, A.L., ALTOBELLI, S.A., FUKUSHIMA, E., MONDY, L.A. & STEPHENS, T.S. 1991 Experimental observations of particle migration in concentrated suspensions: Couette flow. *J. Rheol.* **35** (5), 773–795.

ACRIVOS, A., MAURI, R. & FAN, X. 1993 Shear-induced resuspension in a Couette device. *Intl J. Multiphase Flow* **19** (5), 797–802.

ARSHAD, M., MAALI, A., CLAUDET, C., LOBRY, L., PETERS, F. & LEMAIRE, E. 2021 An experimental study on the role of inter-particle friction in the shear-thinning behavior of non-Brownian suspensions. *Soft Matt.* **17** (25), 6088–6097.

BADIA, A., D'ANGELO, Y., PETERS, F. & LOBRY, L. 2022 Frame-invariant modeling for non-Brownian suspension flows. *J. Non-Newtonian Fluid Mech.* **309**, 104904.

BARNES, H.A. 1989 Shear-thickening ('dilatancy') in suspensions of nonaggregating solid particles dispersed in Newtonian liquids. *J. Rheol.* **33** (2), 329–366.

BATCHELOR, G.K. 1970 The stress system in a suspension of force-free particles. *J. Fluid Mech.* **41** (3), 545–570.

BLANC, F., D'AMBROSIO, E., LOBRY, L., PETERS, F. & LEMAIRE, E. 2018 Universal scaling law in frictional non-Brownian suspensions. *Phys. Rev. Fluids* **3** (11), 114303.

BLANC, F., LEMAIRE, E., MEUNIER, A. & PETERS, F. 2013 Microstructure in sheared non-Brownian concentrated suspensions. *J. Rheol.* **57** (1), 273–292.

BLANC, F., PETERS, F. & LEMAIRE, E. 2011 Experimental signature of the pair trajectories of rough spheres in the shear-induced microstructure in noncolloidal suspensions. *Phys. Rev. Lett.* **107** (20), 208302.

BOYER, F., GUAZZELLI, É. & POULIQUEN, O. 2011 Unifying suspension and granular rheology. *Phys. Rev. Lett.* **107** (18), 188301.

BUTLER, J.E. & BONNECAZE, R.T. 1999 Imaging of particle shear migration with electrical impedance tomography. *Phys. fluids* **11** (8), 1982–1994.

CHAPMAN, B.K 1991 Shear-induced migration phenomena in concentrated suspensions. PhD thesis, University of Notre Dame.

CHATTÉ, G., COMTET, J., NIGUÈS, A., BOCQUET, L., SIRIA, A., DUCOURET, G., LEQUEUX, F., LENOIR, N., OVARLEZ, G. & COLIN, A. 2018 Shear thinning in non-Brownian suspensions. *Soft Matt.* **14** (6), 879–893.

CHÈVREMONT, W., CHAREYRE, B. & BODIGUEL, H. 2019 Quantitative study of the rheology of frictional suspensions: influence of friction coefficient in a large range of viscous numbers. *Phys. Rev. Fluids* **4** (6), 064302.

CHOW, A.W., IWAYIMA, J.H., SINTON, S.W. & LEIGHTON, D.T. 1995 Particle migration of non-Brownian, concentrated suspensions in a truncated cone-and-plate. In *Society of Rheology Meeting, Sacramento, CA, USA*, vol. 103, p. 22.

CHOW, A.W., SINTON, S.W., IWAMIYA, J.H. & STEPHENS, T.S. 1994 Shear-induced particle migration in Couette and parallel-plate viscometers: NMR imaging and stress measurements. *Phys. Fluids* **6** (8), 2561–2576.

CHRISTIANSEN, C. 1884 Untersuchungen über die optischen eigenschaften von fein vertheilten körpern. *Ann. Phys.* **259** (10), 298–306.

COMTET, J., CHATTÉ, G., NIGUÈS, A., BOCQUET, L., SIRIA, A. & COLIN, A. 2017 Pairwise frictional profile between particles determines discontinuous shear thickening transition in non-colloidal suspensions. *Nat. Commun.* **8** (1), 1–7.

COUSSOT, P. & PIAU, J.M. 1994 On the behavior of fine mud suspensions. *Rheol. Acta* **33** (3), 175–184.

DAGOIS-BOHY, S., HORMOZI, S., GUAZZELLI, E. & POULIQUEN, O. 2015 Rheology of dense suspensions of non-colloidal spheres in yield-stress fluids. *J. Fluid Mech.* **776**, R2.

D'AMBROSIO, E., BLANC, F. & LEMAIRE, E. 2021 Viscous resuspension of non-Brownian particles: determination of the concentration profiles and particle normal stresses. *J. Fluid Mech.* **911**, A22.

DBOUK, T., LOBRY, L. & LEMAIRE, E. 2013 Normal stresses in concentrated non-Brownian suspensions. *J. Fluid Mech.* **715**, 239.

DEBOEUF, S., LENOIR, N., HAUTEMAYOU, D., BORNERT, M., BLANC, F. & OVARLEZ, G. 2018 Imaging non-Brownian particle suspensions with X-ray tomography: application to the microstructure of Newtonian and viscoplastic suspensions. *J. Rheol.* **62** (2), 643–663.

DEGIULI, E., DÜRING, G., LERNER, E. & WYART, M. 2015 Unified theory of inertial granular flows and non-Brownian suspensions. *Phys. Rev.* E **91** (6), 062206.

VON EILERS, H. 1941 Die viskosität von emulsionen hochviskoser stoffe als funktion der konzentration. *Kolloid. Z.* **97** (3), 313–321.

ETCHEVERRY, B. 2022 Le capillarytron: un nouveau rhéomètre pour sonder la rhéologie frictionnelle des suspensions colloïdales. PhD thesis, Aix Marseille Université.

GADALA-MARIA, F. & ACRIVOS, A. 1980 Shear-induced structure in a concentrated suspension of solid spheres. *J. Rheol.* **24** (6), 799–814.

GALLIER, S., LEMAIRE, E., LOBRY, L. & PETERS, F. 2016 Effect of confinement in wall-bounded non-colloidal suspensions. *J. Fluid Mech.* **799**, 100–127.

GALLIER, S., LEMAIRE, E., PETERS, F. & LOBRY, L. 2014 Rheology of sheared suspensions of rough frictional particles. *J. Fluid Mech.* **757**, 514–549.

GRAHAM, A.L., ALTOBELLI, S.A., FUKUSHIMA, E., MONDY, L.A. & STEPHENS, T.S. 1991 Note: NMR imaging of shear-induced diffusion and structure in concentrated suspensions undergoing Couette flow. *J. Rheol.* **35** (1), 191–201.

GUAZZELLI, É. & POULIQUEN, O. 2018 Rheology of dense granular suspensions. *J. Fluid Mech.* **852**, P1.

GUY, B.M., HERMES, M. & POON, W.C.K. 2015 Towards a unified description of the rheology of hard-particle suspensions. *Phys. Rev. Lett.* **115** (8), 088304.

HAMPTON, R.E., MAMMOLI, A.A., GRAHAM, A.L., TETLOW, N. & ALTOBELLI, S.A. 1997 Migration of particles undergoing pressure-driven flow in a circular conduit. *J. Rheol.* **41** (3), 621–640.

KOH, C.J., HOOKHAM, P. & LEAL, L.G. 1994 An experimental investigation of concentrated suspension flows in a rectangular channel. *J. Fluid Mech.* **266**, 1–32.

LE, A.V.N., IZZET, A., OVARLEZ, G. & COLIN, A. 2023 Solvents govern rheology and jamming of polymeric bead suspensions. *J. Colloid Interface Sci.* **629**, 438–450.

LEIGHTON, D. & ACRIVOS, A. 1986 Viscous resuspension. *Chem. Engng Sci.* **41** (6), 1377–1384.

LEIGHTON, D. & ACRIVOS, A. 1987 The shear-induced migration of particles in concentrated suspensions. *J. Fluid Mech.* **181**, 415–439.

LHUILLIER, D. 2009 Migration of rigid particles in non-Brownian viscous suspensions. *Phys. Fluids* **21** (2), 023302.

LOBRY, L., LEMAIRE, E., BLANC, F., GALLIER, S. & PETERS, F. 2019 Shear thinning in non-Brownian suspensions explained by variable friction between particles. *J. Fluid Mech.* **860**, 682–710.

MANNEVILLE, S., BÉCU, L. & COLIN, A. 2004 High-frequency ultrasonic speckle velocimetry in sheared complex fluids. *Eur. Phys. J.* **28** (3), 361–373.

MARI, R., SETO, R., MORRIS, J.F. & DENN, M.M. 2014 Shear thickening, frictionless and frictional rheologies in non-Brownian suspensions. *J. Rheol.* **58** (6), 1693–1724.

MARON, S.H. & PIERCE, P.E. 1956 Application of Ree–Eyring generalized flow theory to suspensions of spherical particles. *J. Colloid Sci.* **11** (1), 80–95.

MERHI, D., LEMAIRE, E., BOSSIS, G. & MOUKALLED, F. 2005 Particle migration in a concentrated suspension flowing between rotating parallel plates: investigation of diffusion flux coefficients. *J. Rheol.* **49** (6), 1429–1448.

METZGER, B., RAHLI, O. & YIN, X. 2013 Heat transfer across sheared suspensions: role of the shear-induced diffusion. *J. Fluid Mech.* **724**, 527–552.

MEUNIER, P. & LEWEKE, T. 2003 Analysis and treatment of errors due to high velocity gradients in particle image velocimetry. *Exp. Fluids* **35** (5), 408–421.

MILLS, P. & SNABRE, P. 2009 Apparent viscosity and particle pressure of a concentrated suspension of non-Brownian hard spheres near the jamming transition. *Eur. Phys. J.* E **30** (3), 309–316.

MORRIS, J.F. & BOULAY, F. 1999 Curvilinear flows of noncolloidal suspensions: the role of normal stresses. *J. Rheol.* **43** (5), 1213–1237.

MUELLER, S., LLEWELLIN, E.W. & MADER, H.M. 2010 The rheology of suspensions of solid particles. *Proc. R. Soc. Lond.* A **466** (2116), 1201–1228.

NOTT, P.R. & BRADY, J.F. 1994 Pressure-driven flow of suspensions: simulation and theory. *J. Fluid Mech.* **275**, 157–199.

NOTT, P.R., GUAZZELLI, E. & POULIQUEN, O. 2011 The suspension balance model revisited. *Phys. Fluids* **23** (4), 043304.

OVARLEZ, G., BERTRAND, F. & RODTS, S. 2006 Local determination of the constitutive law of a dense suspension of noncolloidal particles through magnetic resonance imaging. *J. Rheol.* **50** (3), 259–292.

PETERS, F., GHIGLIOTTI, G., GALLIER, S., BLANC, F., LEMAIRE, E. & LOBRY, L. 2016 Rheology of non-Brownian suspensions of rough frictional particles under shear reversal: a numerical study. *J. Rheol.* **60** (4), 715–732.

PHILLIPS, R.J., ARMSTRONG, R.C., BROWN, R.A., GRAHAM, A.L. & ABBOTT, J.R. 1992 A constitutive equation for concentrated suspensions that accounts for shear-induced particle migration. *Phys. Fluids* A **4** (1), 30–40.

PINE, D.J., GOLLUB, J.P., BRADY, J.F. & LESHANSKY, A.M. 2005 Chaos and threshold for irreversibility in sheared suspensions. *Nature* **438** (7070), 997–1000.

QUEMADA, D. 1998 Rheological modelling of complex fluids. I. The concept of effective volume fraction revisited. *Eur. Phys. J.* **1** (1), 119–127.

RICHARDSON, J.F. & ZAKI, W.N. 1954 The sedimentation of a suspension of uniform spheres under conditions of viscous flow. *Chem. Engng Sci.* **3** (2), 65–73.

SAINT-MICHEL, B., MANNEVILLE, S., MEEKER, S., OVARLEZ, G. & BODIGUEL, H. 2019 X-ray radiography of viscous resuspension. *Phys. Fluids* **31** (10), 103301.

SARABIAN, M., FIROUZNIA, M., METZGER, B. & HORMOZI, S. 2019 Fully developed and transient concentration profiles of particulate suspensions sheared in a cylindrical Couette cell. *J. Fluid Mech.* **862**, 659–671.

SCHATZMANN, M., FISCHER, P. & BEZZOLA, G.R. 2003 Rheological behavior of fine and large particle suspensions. *J. Hydraul. Engng ASCE* **129** (10), 796–803.

SEGRE, G. & SILBERBERG, A. 1962 Behaviour of macroscopic rigid spheres in Poiseuille flow. Part 2. Experimental results and interpretation. *J. Fluid Mech.* **14** (1), 136–157.

SINGH, A., MARI, R., DENN, M.M. & MORRIS, J.F. 2018 A constitutive model for simple shear of dense frictional suspensions. *J. Rheol.* **62** (2), 457–468.

SNOOK, B., BUTLER, J. E. & GUAZZELLI, É. 2016 Dynamics of shear-induced migration of spherical particles in oscillatory pipe flow. *J. Fluid Mech.* **786**, 128–153.

SOSIO, R. & CROSTA, G.B. 2009 Rheology of concentrated granular suspensions and possible implications for debris flow modeling. *Water Resour. Res.* **45** (3), W03412.

SOUZY, M., PHAM, P. & METZGER, B. 2016 Taylor's experiment in a periodically sheared particulate suspension. *Phys. Rev. Fluids* **1** (4), 042001.

SOUZY, M., YIN, X., VILLERMAUX, E., ABID, C. & METZGER, B. 2015 Super-diffusion in sheared suspensions. *Phys. Fluids* **27** (4), 041705.

TANNER, R.I. 2018 Aspects of non-colloidal suspension rheology. *Phys. Fluids* **30** (10), 101301.

TAPIA, F., POULIQUEN, O. & GUAZZELLI, E. 2019 Influence of surface roughness on the rheology of immersed and dry frictional spheres. *Phys. Rev. Fluids* **4** (10), 104302.

TRULSSON, M., DEGIULI, E. & WYART, M. 2017 Effect of friction on dense suspension flows of hard particles. *Phys. Rev.* E **95** (1), 012605.

VANCE, K., SANT, G. & NEITHALATH, N. 2015 The rheology of cementitious suspensions: a closer look at experimental parameters and property determination using common rheological models. *Cement Concrete Comp.* **59**, 38–48.

VINCENT, L. & SOILLE, P. 1991 Watersheds in digital spaces: an efficient algorithm based on immersion simulations. *IEEE Comput. Archit. Lett.* **13** (6), 583–598.

WESTERWEEL, J. 1997 Fundamentals of digital particle image velocimetry. *Meas. Sci. Technol.* **8** (12), 1379–1392.

WILDEMUTH, C.R. & WILLIAMS, M.C. 1984 Viscosity of suspensions modeled with a shear-dependent maximum packing fraction. *Rheol. Acta* **23** (6), 627–635.

WYART, M. & CATES, M.E. 2014 Discontinuous shear thickening without inertia in dense non-Brownian suspensions. *Phys. Rev. Lett.* **112** (9), 098302.

YEO, K. & MAXEY, M.R. 2010 Ordering transition of non-Brownian suspensions in confined steady shear flow. *Phys. Rev.* E **81** (5), 051502.

ZARRAGA, I.E., HILL, D.A. & LEIGHTON, D.T., JR. 2000 The characterization of the total stress of concentrated suspensions of noncolloidal spheres in Newtonian fluids. *J. Rheol.* **44** (2), 185–220.

ZHOU, J.Z.Q., UHLHERR, P.H.T. & LUO, F.T. 1995 Yield stress and maximum packing fraction of concentrated suspensions. *Rheol. Acta* **34** (6), 544–561.